

Observations of gravity waves in the middle atmosphere of Mars

WILLIAM R. SAUNDERS ,¹ MICHAEL J. PERSON ,² AND PAUL WITHERS ,^{1,3}

¹*Department of Astronomy, Boston University, Boston, MA 02215, USA*

²*Department of Earth, Atmospheric, and Planetary Sciences, Massachusetts Institute of Technology (MIT), Cambridge, MA 02139-4307, USA.*

³*Center for Space Physics, Boston University, Boston, MA 02215, USA*

(Received April 17, 2020; Revised March 22, 2021; Accepted *****)

Submitted to AJ

ABSTRACT

Gravity waves are ubiquitous throughout the atmosphere of Mars. Their propagation and dissipation influence the circulation and thermal structure of the middle and upper atmosphere. Yet there have been few studies of gravity wave characteristics in the middle atmosphere, a region that is critical for their propagation from generation in the lower atmosphere to dissipation and associated exchanges of momentum and energy in the upper atmosphere. There have been few studies because few atmospheric profiles span the middle atmosphere with the vertical resolution of km-scale or smaller that is required to characterize gravity waves.

Here we report the characterization of gravity waves in the middle atmosphere using twelve high-resolution atmospheric density profiles. Four of these were acquired from a ground-based stellar occultation from 1976 that yielded immersion and emersion profiles on opposite sides of the planet and the remaining eight were measured during

22 atmospheric entry by landers and rovers.

23 Predominant wavelengths were 3–14 km and amplitudes were generally 0.8%–2.5%.

24 Where static stability is large and positive, gravity waves grow efficiently. In other
25 instances, static stability is not large and positive over a wide altitude range, and
26 gravity wave amplitudes do not behave as neatly.

27 These observations of gravity waves in the middle atmosphere of Mars can be used
28 to test gravity wave parameterizations in large-scale general circulation models and to
29 investigate predictions for how gravity wave propagation and dissipation influence the
30 circulation and thermal structure of the middle and upper atmosphere.

31 *Keywords:* Mars, planetary atmospheres, stellar occultation, gravity waves

32 1. INTRODUCTION

33 Internal gravity waves are common atmospheric waves that propagate vertically upwards in fluid,
34 stably stratified planetary atmospheres (Fritts & Alexander 2003; Yiğit & Medvedev 2015). They are
35 associated with the adiabatic displacement of air parcels that are restored to their original positions
36 by buoyancy forces. Gravity waves are distinguished from physically-similar oscillations (e.g., Rossby
37 waves, thermal tides) by their small horizontal scales (much less than a planetary radius) and short
38 periods (much less than a planetary rotation period) (England et al. 2017). Gravity waves can
39 be generated by flow over topography, convective processes, wind shear, weather fronts, and other
40 sources (Fritts & Alexander 2003; Yiğit & Medvedev 2015). These sources are usually located at
41 tropospheric altitudes but waves can be generated at higher altitudes by local convective instabilities.

42 Gravity waves are important for vertical coupling within a planetary atmosphere. Propagating
43 gravity waves carry vertical fluxes of horizontal momentum and energy, but not mass. Conservation
44 of energy dictates that, in the absence of dissipation, gravity wave amplitudes increase with increasing
45 altitude as atmospheric mass density decreases. This trend is disrupted where waves break, dissipate,
46 or saturate. Wave breaking or dissipation, the former term reserved for more violent amplitude
47 decrease, results in depositing momentum and energy into the local atmosphere in a narrow vertical

48 altitude range. Saturation describes a wave whose amplitude neither increases nor decreases with
49 altitude ([Fritts & Alexander 2003](#)).

50 This transport of momentum and energy from the lower atmosphere to higher altitudes influences
51 the mean circulation and thermal structure of these higher altitude regions. Gravity waves can
52 influence dynamics by slowing or reversing mean flows in the upper atmosphere. The adiabatic
53 perturbations of the waves create local temperature fluctuations even in regions where the waves
54 propagate stably. Where gravity waves dissipate and/or break, the deposition of energy may ei-
55 ther increase or decrease atmospheric temperatures, depending on the local atmosphere conditions.
56 Gravity waves also contribute to turbulent mixing of the atmosphere. Furthermore, gravity waves
57 contribute to stochastic atmospheric variability in these higher altitude regions.

58 On Earth, gravity waves influence mesospheric circulation and associated winter polar warming, ini-
59 tiate sudden stratospheric warming events, and excite the quasi-biennial oscillation ([Fritts & Alexan-](#)
60 [der 2003; Yiğit & Medvedev 2015](#)). On Mars, gravity waves affect middle atmospheric circulation
61 and associated winter polar warming ([Barnes et al. 2017; Gilli et al. 2020; Heavens et al. 2020](#)). They
62 may also create localized cold pockets that promote the condensation of CO₂ ice clouds ([Spiga et al.](#)
63 [2012a](#)). They can cause large density variations in the thermosphere which affect the homopause
64 location. As these waves dissipate, they modify the background thermal structure of the atmosphere.
65 In the mesosphere and thermosphere, the cooling effects of gravity waves are comparable to the ef-
66 fects of the primary radiative mechanism, infra-red radiation by CO₂ molecules ([Smith et al. 2017;](#)
67 [Gilli et al. 2020; Heavens et al. 2020](#)). The effects of gravity waves appear to be more impactful
68 on Mars than on Earth, modifying circulation and atmospheric structure significantly ([Gilli et al.](#)
69 [2020; Heavens et al. 2020; Gubenko et al. 2015](#)). This is consistent with Mars having significantly
70 greater topographic variations than Earth and a lower Brunt-Väisälä (buoyancy) frequency on aver-
71 age. Moreover, gravity waves on Mars have been detected with larger amplitudes and broader spectra
72 than on Earth ([Gubenko et al. 2015](#)).

73 Gravity waves on Mars that affect thermospheric conditions are generated in the lower atmosphere,
74 but the dependences of gravity wave activity on latitude and time of day differ between the lower

atmosphere and the thermosphere. Activity is greatest in the tropics in the lower atmosphere (Creasey et al. 2006a; Ando et al. 2012; Tellmann et al. 2013a; Heavens et al. 2020), but smallest in the tropics in the thermosphere (Creasey et al. 2006b; Fritts et al. 2006; Withers 2006; England et al. 2017; Yiğit et al. 2015; Vals et al. 2019; Terada et al. 2017). Gravity wave amplitudes are greatest on the cold nightside in the thermosphere (England et al. 2017). Relationships between gravity wave activity in the thermosphere and in the lower atmosphere are influenced by the propagation of gravity waves through the intervening middle atmosphere. Observations of gravity waves in the middle atmosphere can offer valuable insight into gravity wave propagation and dissipation, thereby contributing to improved understanding of how gravity waves affect the circulation and thermal structure of the middle and upper atmosphere. Yet observations of gravity waves in this critical middle atmosphere region are extremely rare.

Consequently, many important questions about the behavior of gravity waves in the middle atmosphere of Mars remain unresolved. What are the characteristic wavelengths of gravity waves in the middle atmosphere? What are the amplitudes of gravity waves in the middle atmosphere? How does gravity wave amplitude change with altitude in the middle atmosphere? What seasonal and diurnal variations impact the location, strength, and amplitudes of gravity waves?

In order to advance understanding of the role of gravity waves in the atmosphere of Mars, the aim of this report is to characterize small-scale structure in atmospheric profiles at middle atmospheric altitudes. This aim will be achieved by analysis and interpretation of two types of data: Earth-based observations of the occultation of the bright star ϵ Geminorum by Mars in 1976 and entry profiles from Vikings 1 and 2, Pathfinder, Spirit, Opportunity, Phoenix, Curiosity, and InSight.

The structure of this article is as follows. Section 2 introduces gravity waves in the atmosphere of Mars. Section 3 introduces the stellar occultation method for measuring atmospheric profiles. Section 4 describes the 1976 occultation of ϵ Geminorum by Mars. Section 5 describes how high-resolution atmospheric profiles were obtained from this occultation in a reanalysis of archival data. Section 6 assesses and validates these occultation profiles. Section 7 introduces the aerodynamic drag method for measuring atmospheric profiles during a spacecraft's atmospheric entry. Section 8 characterizes

102 the small-scale structure present in both types of atmospheric profile. Section 9 interprets the findings
103 of Section 8. Section 10 discusses the behavior of gravity waves in the middle atmosphere of Mars.
104 Section 11 presents the conclusions of this work.

105 2. GRAVITY WAVES IN THE ATMOSPHERE OF MARS

106 Gravity waves on Mars have primarily been observed via their effects on atmospheric density,
107 pressure, and temperature profiles. Such profiles have been acquired by several different types of
108 instruments, including radio occultations, infra-red limb sounders, ultraviolet stellar occultations,
109 and *in situ* density measurements from orbiters and landers. Earth-based observations of stellar
110 occultations can also provide such profiles.

111 Radio occultation observations provide vertical profiles of atmospheric density, pressure, and tem-
112 perature between the surface and approximately 40 km altitude with vertical resolution of \sim 1 km.
113 Creasey et al. (2006a) analyzed radio occultation profiles from Mars Global Surveyor. They used
114 variations in temperature around the background state to determine the gravity wave potential en-
115 ergy per unit mass at 10–30 km altitude. In order to exclude long-wavelength thermal tides, they
116 filtered these profiles to eliminate oscillations with vertical wavelengths greater than 10 km. They
117 found that the potential energy was greatest in the tropics, notably over the Tharsis rise, with a
118 maximum value on the order of 10 J kg^{-1} . Values outside the tropics were less than 2 J kg^{-1} . Ando
119 et al. (2012) analyzed the same dataset to characterize the spectrum of gravity waves (i.e., domi-
120 nant vertical wavelengths) at 3–32 km altitude. This analysis was sensitive to wavelengths in the
121 range 2.5 km to 15 km. At wavelengths less than 8 km, they found that spectral power increased
122 as wavelength increased. Furthermore, they found that the quantitative expression of this relation-
123 ship, a power law, was consistent with terrestrial experience and theoretical expectations. At longer
124 wavelengths, the spectral slope is markedly flatter. They attributed this to the presence of thermal
125 tides. In addition, Ando et al. (2012) confirmed that gravity wave power is greatest in the tropics.
126 Tellmann et al. (2013a) analyzed radio occultation profiles from Mars Express at 0–40 km altitude.
127 They also examined variations in temperature around the background state and filtered their results
128 to eliminate oscillations with vertical wavelengths greater than 10 km, which were deemed to be

129 influenced by thermal tides. Tellmann et al. (2013a) reported that wave amplitudes increased with
130 increasing altitude, as expected. However, they found that this exponential growth ceased at \sim 33
131 km altitude, implying wave breaking at this altitude. They also noted that gravity wave activity was
132 strongest around Tharsis. Here the amplitude of the temperature fluctuations reached \approx 6 K around
133 30–40 km altitude.

134 Infra-red limb sounding observations provide temperature-pressure profiles in the lower and middle
135 atmosphere. MGS TES profiles from limb sounding generally extend from the surface to \sim 60 km
136 altitude and the vertical resolution is approximately 10 km (Smith et al. 2001). Due to this coarse
137 resolution, few gravity wave studies have been conducted with MGS TES profiles. Feofilov et al.
138 (2012) were able to extend a small fraction of these profiles up to \sim 90 km. They noted strong
139 profile-to-profile variability in their set of observations. They attributed this to gravity waves and
140 reported that the root-mean-square of the temperature variability was 7 K at 60 km, 11 K at 70
141 km, 18 K at 80 km, and 25 K at 90 km. MRO MCS profiles generally extend from the surface to
142 \sim 80 km altitude with vertical resolution of \sim 5 km. Wright (2012) analyzed temperature fluctuations
143 in MCS profiles and filtered their results to eliminate oscillations with vertical wavelengths greater
144 than 10 km, which were deemed to be influenced by thermal tides. They found that wave amplitude
145 decreased with increasing altitude from tens of Kelvin at 2 mbar (\sim 5 km altitude) to <1 K at 0.1
146 mbar (\sim 50 km altitude). Similarly, Creasey et al. (2006a) identified gravity waves decreasing in
147 amplitude between 5 km and 35 km altitude using MGS radio occultation, which they attributed to
148 saturation. Heavens et al. (2020) analyzed variations in MCS on-planet radiance observations, which
149 they deemed to have been caused by gravity waves. This analysis was most sensitive to gravity
150 waves with vertical wavelengths of 10 km or greater. Their use of on-planet (i.e., nadir or close to
151 nadir) observations, as opposed to limb sounding observations, provided sensitivity to gravity waves
152 with horizontal wavelengths of 10–30 km, unlike the hundreds of kilometers characteristics of limb
153 sounding methods. They confirmed the association of gravity waves with topographic features and
154 also noted that the power of topographically-driven gravity waves is intermittent. They reported
155 that gravity wave activity was increased by regional and global dust storms.

UV stellar occultation observations provide vertical profiles of atmospheric density, pressure, and temperature in the middle and upper atmosphere. Mars Express SPICAM profiles extend from 70 km altitude to 130 km altitude with vertical resolution of \sim 3 km. The temperature uncertainty varies with altitude, but a characteristic value is 10 K. These profiles are generally smooth and show little indication of the presence of gravity waves (Montmessin et al. 2006; Quémérais et al. 2006; Forget et al. 2009; Withers et al. 2011). MAVEN IUVS profiles have slightly smaller temperature uncertainties (\sim 5 K) than those of SPICAM, but show similarly little indications of gravity waves. Instead, longer-wavelength variations attributed to thermal tides are common (Gröller et al. 2018).

Earth-based observations of stellar occultations provide vertical profiles of atmospheric density, pressure, and temperature in the middle atmosphere. The 1976 occultation of ϵ Geminorum by Mars provided two atmospheric profiles from \sim 50 km to \sim 90 km altitude with \sim 1 km vertical resolution, but small-scale variations in these profiles were not characterized in detail by the original experimenters (Elliot et al. 1977b).

In situ density measurements at thermospheric altitudes also display signatures of gravity waves. Aerobraking accelerometer observations have been analyzed by several authors. Fritts et al. (2006) found horizontal wavelengths of 20–200 km and density amplitudes of 5%–50%. Creasey et al. (2006b) found horizontal wavelengths of 100–300 km. They also noted that the amplitudes of density fluctuations were not appreciably greater in the tropics than at other latitudes. Withers (2006) found that the amplitudes of density fluctuations were smaller in the tropics than at other latitudes. This is in contrast to results at tropospheric altitudes that show greater gravity wave activity in the tropics. MAVEN neutral mass spectrometer (NGIMS) observations have also been analyzed by several authors. Yiğit et al. (2015) reported density variations of 20–40% at 180–220 km altitude. England et al. (2017) found that the amplitude of density fluctuations depended on species mass. Mass-dependent behavior of the effects of gravity waves was previously seen at Venus and Earth. These amplitudes were anti-correlated with the background atmospheric temperature, such that variations were larger on the nightside than the dayside. Below 205 km, fluctuations in CO₂ density presented horizontal wavelengths on the order of 200 km and amplitudes of roughly 5%–25%. Terada

et al. (2017) also reported density fluctuations of 10%–20% with amplitudes being anti-correlated with the background atmospheric temperature. Hence, nightside amplitudes were greater than dayside amplitudes. Siddle et al. (2019) found density fluctuations of \sim 10% and vertical wavelengths of 10–30 km. Amplitudes increased from the dayside to the nightside, as seen by England et al. (2017).

The entry, descent, and landing of spacecraft on the surface of Mars provide vertical profiles of atmospheric density, pressure, and temperature between \sim 10 km and \sim 120 km altitude with sub-km resolution. Magalhães et al. (1999) reported oscillations in temperature with vertical scales of \sim 5 km and amplitudes of \sim 2–3 K at 80–120 km altitude in the Pathfinder entry profile. Small-scale variations are present in similar profiles from Vikings 1 and 2, Spirit, Opportunity, Phoenix, Curiosity, and InSight (Seiff & Kirk 1976; Withers & Smith 2006; Withers & Catling 2010; Holstein-Rathlou et al. 2016; Banfield et al. 2020), but have not been characterized in detail.

In the lower atmosphere, gravity waves have been observed with km-scale vertical resolution by radio occultations. In the upper atmosphere, gravity waves have been observed with km-scale vertical resolution by in situ density measurements from aerobraking accelerometers and orbiting mass spectrometers. In the middle atmosphere, however, observations of gravity waves with km-scale vertical resolution are rare. Infra-red limb sounders like MGS TES and MRO MCS provide profiles with vertical resolution of 5–10 km. Ultraviolet stellar occultations from MEX SPICAM and MAVEN IUVS provide profiles with vertical resolution of \sim 3 km, but temperature uncertainties of 5–10 K mask the small temperature fluctuations caused by gravity waves.

3. STELLAR OCCULTATIONS

The technique of stellar occultations has been used for over half a century to observe solar system atmospheres with high spatial resolution (Baum & Code 1953; Elliot & Olkin 1996).

As a solar system object with a fluid atmosphere passes across the line of sight from an observer (usually on Earth) to a star, the observed flux from the star is gradually reduced. The flux is impacted by three factors: atmospheric refraction, atmospheric lensing, and extinction by absorption of scattering. The time series of stellar flux from an occultation is called a light curve. Refraction

sets the overall shape of the light curve, with significant contributions from lensing and extinction depending on conditions (Elliot & Young 1992; Chamberlain & Elliot 1997).

Immersion (also called “ingress”) is the beginning of the occultation, when the solar system object moves into the line of sight from the observer to the star. Emersion (also called “egress”) is the end of the occultation, when the solar system object moves out of the line of sight from the observer to the star. The central flash is a brief, yet sometimes intense, enhancement in flux in the middle of the occultation caused by simultaneous refraction around the limb of the solar system object as the star is nearly directly behind the object from the perspective of the observer. This is somewhat analogous to the “Einstein ring” effect in gravitational lensing. It only occurs when the chord of the star across the occulting object passes close to the centroid of the occulting disk. Its exact shape is determined by the atmospheric oblateness and orientation of the occultation geometry (Elliot & Olkin 1996).

Stellar occultations by planetary atmosphere provide temperature, pressure, and number density profiles of the occulting atmospheres with vertical resolution of a few kilometers. The cadence of observations sets the vertical resolution and the brightness difference between the star and planet sets the signal-to-noise of the observation. Stellar occultations are typically most sensitive to the μ bar pressure level, spanning a vertical region of approximately five pressure scale heights. For Mars, this is the middle atmospheric region (Elliot & Olkin 1996).

Occultation light curves also provide the oblateness of a planetary atmosphere, either from multiple chords across an object or from analysis of the central flash. For the giant planets, this oblateness can be used to investigate zonal wind patterns.

4. THE 1976 OCCULTATION OF ϵ GEMINORUM BY MARS

The 8 April 1976 occultation of ϵ Geminorum, a relatively bright star (V-band magnitude of 3.1), by Mars was observed by groups at several locations around the United States and the Kuiper Airborne Observatory (KAO) (Elliot et al. 1977a,b; French & Elliot 1979; French & Taylor 1981; Hubbard 1982; Keenan & McNeil 1989). During the occultation, the KAO was 12.5 km above the Atlantic Ocean, several hundred miles east of North Carolina, USA, at 36°N, 290°E (Elliot et al. 1976). At 12.5 km altitude, the KAO 91 cm telescope observed roughly three times higher signal-to-noise than what

a comparable instrument would have observed on the ground (Young 1967). This occultation was particularly noteworthy in that the group aboard the KAO reported the first central flash observed in a stellar occultation.

These observations were acquired at Ls=52° in Mars Year 12 (Clancy et al. 2000). The immersion profile sampled the atmosphere of Mars at 27°S, 29°E at a local solar time of 3.5 hours. The emersion profile sampled 28°N, 208°E at a local solar time of 15.5 hours. These profiles extended from ~50 km to ~90 km altitude, or pressure levels of 0.1–100 microbars. “The mean temperature is ~145 K, and the profiles exhibit wavelike structures with a peak-to-peak amplitude of 35 K and a vertical scale of about 20 km” (Elliot et al. 1977b). These long-wavelength fluctuations were interpreted as being caused by thermal tides. The results were broadly consistent with the Viking Lander 1 and 2 entry profiles that were obtained in July and September 1976, respectively (Seiff & Kirk 1976).

Data were observed with a 4 ms cadence on photomultiplier tubes. In the original analysis of these occultation light curves, the authors chose to bin the data by a factor of 25 to reduce computation time (Elliot et al. 1977b). This also resulted in a reduction of vertical resolution. Though the published results had a vertical resolution of 1–2 km, this was insufficient to resolve gravity waves because subsequent points produced by the inversion process are highly correlated (see Section A). This means a vertical spacing between points of 1–2 km is insufficient to detect temperature perturbations of a size of similar magnitude.

The original atmospheric profiles obtained from the KAO observations have been lost. However, the raw data still exist.

5. REANALYSIS OF THE ϵ GEMINORUM OCCULTATION

5.1. *Data Calibration*

The raw data from the observation are shown in Figure 1, which indicates a decreasing sensitivity of Channel 1 over time. Unfortunately, any calibration data obtained is undocumented and the instrument is long since destroyed, so we were unable to ascertain the cause of this baseline trend. Given that the trend is apparent only in one of the channels, we suspect without conclusive evidence,

that it was the result of a saturation in that photomultiplier. Regardless of the cause, we fit the data away from occultation to a linear trend and subtract the baseline trend to correct for it. Quadratic and exponential fits were also tested but both converge to nearly linear fits. Therefore, for the rest of this analysis, we stick to the linear fit.

Following the same procedure as [Elliot et al. \(1977b\)](#), we normalize the three channels such that the flux at the upper baseline is assigned a value of 1.0 and the flux during the occultation is assigned a value of 0.0. The upper baseline and occultation levels were assessed by taking the median of symmetric portions of the light curves, avoiding immersion, emersion, and the central flash. Figure 2 shows the normalized light curves of all three channels and Figure 3 highlights the immersion and emersion portions of the normalized light curves, showing finer detail.

The data were recorded in 4 ms integrations. As mentioned, the original work of [Elliot et al. \(1977b\)](#) used data binned to 0.1 s resolution, a factor of 25 decrease in temporal resolution. This choice was taken to limit the processing time of observations to match computational resources available. As those constraints are no longer true today, we use the full 4 ms resolution data, which ensures the best possible vertical resolution.

5.2. *Model Fitting*

The process of determination of atmospheric density, pressure, and temperature profiles from occultation data requires some preparatory work. First, the location of the upper boundary of the resultant atmospheric profile must be selected. This requires the selection of the corresponding flux level, which involves a compromise between the desire to extend the profile as high as possible and the requirement that the diminution in flux caused by the atmosphere be discernible despite experimental noise. Second, the atmospheric conditions at this upper boundary must be specified.

To fulfill these requirements, an idealized atmospheric model is fitted to the data. We use the model fitting procedure of [Elliot & Young \(1992\)](#). We assume a clear atmosphere, thereby neglecting possible extinction by haze and dust. The Mars atmosphere is generally clear at this season ($Ls=52^\circ$). Furthermore, dust and haze are rarely found on Mars at altitudes beyond a few km above the surface ([Montabone et al. 2015](#)). We assume an isothermal atmosphere. As the role of model fitting is to

provide a boundary condition, an isothermal model is sufficient and standard (see e.g., Pasachoff et al. 2016; Bosh et al. 2015; Person et al. 2008, 2013; Person et al. 2019). Furthermore, the middle atmosphere of Mars does not usually contain such exceptionally strong thermal gradients as to invalidate this assumption (Smith et al. 2017).

Fitting the immersion portion of the light curve yielded the isothermal scale height for that location. The typical approach is to fit the model to the high altitude portion of the light curve only. For example, Elliot et al. (1977b) fitted down to a flux level of 0.7. The full inversion then begins at that flux level. However, here we elected to fit the model to the entire immersion portion of the light curve and to begin the full inversion at the relatively high flux level of 0.9. The benefits of doing so are two-fold: one, we find a more reliable globally-averaged temperature measurement. Two, by starting at a higher flux level, we can perform a protracted search for wave activity over a larger vertical region of the atmosphere. The emersion portion of the light curve was fitted similarly.

We also fit an atmospheric model to the central flash portion of the light curve. As discussed in Section 3, deep stellar occultations have a central flash feature. This is caused by simultaneous refraction of starlight around the limb of the occulting body as the center of the occulting body passes relatively close to the line of sight between the observer and the star. The KAO flight plan was designed to bring the observer-star line of sight as close to the center of Mars as possible. Hence the ϵ Geminorum occultation has a strong central flash with two peaks that can be seen in Figure 2. The intensities of these two peaks are primarily determined by the impact parameter (the distance from the occultation chord to the centroid of the occultation shadow) and the atmospheric oblateness. We fit the Elliot & Young (1992) model to the central flash portion of the light curve. Note that Elliot et al. (1977b) did not have a robust model fitting approach to the central flash. Instead, they determined the impact parameter using forward modeling and evaluated their candidate fits by eye.

The immersion, emersion, and central flash model fits are shown in Figure 4 and the parameters resulting from the fits are outlined in Table 1. The immersion and emersion scale height values are consistent with previous findings (Kieffer et al. 1992). The atmospheric ellipticity value is roughly

315 a factor of two lower than the solid body ellipticity of Mars. The goodness-of-fit parameters are
316 acceptable.

317 The best model fit to the central flash may appear by eye to not fully fit the trends in the data.
318 This is due to systematic uncertainties. For example, the model does not account for a dip in flux
319 before the central flash, as can be seen at 1795 seconds in the middle panel of Figure 4. It is possible
320 that this dip is due to atmospheric structure that the central flash model of [Elliot & Young \(1992\)](#)
321 does not include and therefore the fit is worse than captured by the reported errors.

322 Another source of systematic error is that the central flash fitting relies on the fitting results to
323 immersion and emersion. For instance, a small error in the value of occultation mid-time when
324 fitting the immersion and emersion curves may be introduced due to photon noise. Though it hardly
325 affects the fit of the limbs, this error applied to the central flash may cause the model to vary
326 other parameters in an attempt to correct a slightly incorrect mid-time. The result is systematic
327 uncertainties that are grossly underestimated by the random uncertainties reported in Table 1. A 10
328 km uncertainty on the impact parameter is more realistic, which results in an approximately 10 km
329 uncertainty in altitude.

330 In data collected during an occultation today, these uncertainties would not be acceptable. Modern
331 GPS and planetary ephemerides make it possible to astrometrically solve for the occultation geometry.
332 The KAO position was recorded by inertial sensors during observations, which identified a 2 arcminute
333 discrepancy in latitude and longitude upon landing ([Elliot et al. 1977b](#)). Furthermore, running
334 modern ephemerides four decades back in time introduces difficult-to-calibrate uncertainties. Given
335 these constraints, we accept the \sim 10 km vertical uncertainty and reiterate that it does not materially
336 impact the findings of this work. We express vertical altitude primarily in terms of pressure and
337 otherwise only use relative altitude comparison.

338 5.3. *Inversion*

339 In this reanalysis, we follow the inversion procedure outlined in [Elliot, Person, & Qu \(2003\)](#), which
340 is the seminal work on the modern approach to the [French et al. \(1978\)](#) inversion procedure used in
341 the original work. The details of the inversion process are summarized in Appendix A. We assume the

boundary conditions reported in Table 1. Note that the upper boundary conditions determined by model fitting (Section 5.2) were influenced by atmospheric properties above and below this boundary. While it is formally undesirable that atmospheric properties below the upper boundary influence the upper boundary conditions, the negative consequences of this are minor.

The inversion approach assumes that refracted light rays do not cross (Appendix A). A corollary of this is that all normalized flux values used in the inversion must be positive because a negative normalized flux value implies a degeneracy in parameter space that cannot be resolved with these observations alone. Some of the full-resolution normalized flux values are negative due to noise, which is resolved by binning data points as needed to ensure positive normalized flux values (Elliot et al. 2003).

If the inversion procedure encounters a negative normalized flux value as it advances downwards in altitude, it averages it with the requisite number of subsequent points to create a positive normalized flux value. The effect is the same as binning, but this method applies the minimum binning possible at each point rather than a consistent bin size everywhere, which preserves as much of the vertical resolution as possible.

The lower boundary of the atmospheric profile is set by noise. Inversion ends either when the binning becomes too large to perform analysis or when the measured flux values are dominated by photon noise and no longer represent real atmospheric structure. In our reanalysis, observations are limited to the middle Martian atmosphere in the pressure range $0.1 \mu\text{bar} \lesssim p \lesssim 10 \mu\text{bar}$ (50 km $\lesssim z \lesssim 95$ km), where p is pressure. This approximately corresponds to the same altitude range of the original analysis.

6. RESULTS FROM REANALYSIS OF THE OCCULTATION OBSERVATIONS

6.1. *Issues of Altitude*

The primary data products of this work are two vertical profiles of number density, pressure, and temperature of the Martian middle atmosphere. Occultation profiles are formally determined in terms of radial distance (see Section 5.3). We converted our radial distances to altitude by subtracting the

appropriate radius of the areoid (gravitational equipotential surface) produced by the Mars Orbiter Laser Altimeter (MOLA) experiment aboard the Mars Global Surveyor (MGS) spacecraft (Lemoine et al. 2001). At the latitudes and longitudes of the immersion and emersion profiles, the areoid radius is 3391.8 km and 3392.3 km, respectively. This reference areoid was not available to Elliot et al. (1977b), who instead converted radial distances to altitudes by subtracting 3401 ± 5 km and 3404 ± 7 km, respectively, from their immersion and emersion radial distances.

Comparison of pressure-altitude profiles (not shown) from our reanalysis and the original results of Elliot et al. (1977b) revealed unexpected discrepancies. Pressure decreases roughly exponentially with increasing altitude. Yet our pressure-altitude profiles and those of Elliot et al. (1977b) were offset by approximately 10 km on both immersion and emersion.

As explained in Section 5.2, we expect a discrepancy of this order due to the systematic uncertainties of fitting a model to the central flash feature. The approximately 10 km uncertainty in the impact parameter translates to a similar uncertainty in the radial distances of each data point in the profile. Note that this source of error affects the absolute values of radial distance. It does not affect relative radial distances or altitudes in a given profile. Our reanalysis and the analysis of Elliot et al. (1977b) adopted different values for the impact parameter, which leads to differences in radial distance.

We introduced additional information to resolve this discrepancy. The Mars Climate Database (MCD) (Millour et al. 2019) is a robust general circulation model benchmarked with *in situ* and remote sensing measurements from current and former missions to Mars. We compared pressure-altitude profiles from our reanalysis and from Elliot et al. (1977b) to relevant output from the MCD, then found the altitude adjustment necessary to bring each occultation profile into alignment with the relevant MCD profile.

We adjusted the nominal values of altitude in the immersion and emersion profiles of Elliot et al. (1977b) by 4 km and 7 km, respectively. Similarly, we adjusted the nominal values of altitudes in our immersion and emersion reanalysis profiles by 14 km and 15 km, respectively. As mentioned above, these altitude adjustments differ between the original analysis and this work due to different

394 calculated impact parameters and definitions of the surface of Mars. Note that this adjustment does
395 not affect temperature-pressure profiles (Section 6.2) or the wave analysis of subsequent sections.

396 *6.2. Atmospheric Profiles*

397 Figure 5 shows the immersion and emersion temperature-pressure profiles from the channel 2 and
398 channel 3 light curve data. Close inspection of data from channel 1 reveals that it has significantly
399 worse signal-to-noise than the other channels, so we neglect results from channel 1 in the remainder
400 of this article.

401 Figure 5 also shows the versions of these profiles that were obtained in the original analysis of
402 Elliot et al. (1977b). The numerical results have been lost, so we recovered these profiles from the
403 published work using the graphClick software. Relevant figures in Elliot et al. (1977b) showed
404 pressure as a function of altitude and temperature as a function of altitude, but not temperature as
405 a function of pressure. We combined results recovered from these two representations to obtain the
406 temperature-pressure profiles shown in Figure 5. Figure 5 also shows simulated atmospheric profiles
407 from the MCD.

408 Figure 5 includes altitude as a secondary axis. As the corresponding pressure-altitude profiles for
409 the five temperature-pressure profiles included in this figure are formally different, the altitude axis
410 is approximate.

411 *6.3. Validation of the Atmospheric Profiles*

412 Our reanalysis profiles are generally similar to the original results of Elliot et al. (1977b). Mean
413 temperatures are similar and large-scale structures are similar. Furthermore, the channel 2 and
414 channel 3 immersion profiles are more self-consistent in our reanalysis than in Elliot et al. (1977b).
415 Our emersion profiles are also more self-consistent than those of Elliot et al. (1977b). These outcomes
416 are encouraging for the validity of the results of our reanalysis.

417 For immersion, the mean temperatures in the reanalysis profile and the MCD profile are consistent.
418 Furthermore, the wavelengths and amplitudes of large-scale structure in temperature are also similar
419 in the reanalysis profile and the MCD profile. In the reanalysis immersion profile, the characteristic

wavelength is around 23 km and the characteristic peak-to-peak amplitude is around 30 K. In the MCD immersion profile, the corresponding values are 30 km and 25 K. Yet the phasing of temperature extrema are not particularly consistent between these two profiles. The reanalysis immersion profile has a temperature maximum of 162 K at 0.72 μ bar, whereas the MCD immersion profile has a temperature maximum of 161 K at 2.0 μ bar. The reanalysis immersion profile has a temperature minimum of 128 K at 2.3 μ bar, whereas the MCD has a temperature minimum of 136 K at 12.3 μ bar (below the bottom of Figure 5a). For emersion, the reanalysis profile agrees well with the corresponding MCD profile.

Overall, the reanalysis profiles are more self-consistent than the original profiles. Moreover, the reanalysis profiles are at least as consistent with the MCD profiles as the original profiles are. We conclude that the reanalysis profiles are acceptable for scientific interpretation.

6.4. *Distinctive Features of the Atmospheric Profiles*

Mean temperatures are similar in the immersion and emersion profiles, approximately 150 K. Long-wavelength structure is present in both profiles. Vertical wavelengths are similar in both profiles, (\sim 20–25 km), but the peak-to-peak amplitude is greater in the immersion profile (\sim 30 K) than in the emersion profile (\sim 10 K). We concur with the assessment of the original observers that this long-wavelength structure is likely caused by thermal tides. Short-wavelength structure is also present in both profiles at a vertical wavelength of roughly 5 km. This is evident in, for example, the channel 2 emersion profile around 1 μ bar pressure (Figure 5).

As outlined in Section 2, these fluctuations are likely to be caused by gravity waves. They are not apparent to the naked eye in the original profiles. As the original profiles averaged the raw 4 ms data to 0.1 seconds, their vertical resolution is 1 km. As detailed in Section 4, 1 km vertical resolution in an occultation is typically insufficient to observe variations on the same order of magnitude.

As averaging was not required for the reanalysis profiles, we produce better vertical resolution of 0.01–0.1 km. This improvement in vertical resolution renders small-scale structure much more visible.

7. ENTRY PROFILES

Spacecraft enter atmospheres at speeds comparable to orbital speeds. Typical values are several kilometers per second, much greater than the speed of sound in planetary atmospheres (Houghton 2002). A spacecraft entering a planetary atmosphere at hypersonic speed decelerates due to atmospheric drag (Withers et al. 2003b). Momentum is transferred from the spacecraft to the atmosphere at a rate which can be estimated from the principle of conservation of momentum. The spacecraft of area A traveling at speed v sweeps through a volume $Av\Delta t$ of atmospheric gas in time Δt . The mass of this amount of air is $\rho Av\Delta t$, where ρ is the local atmospheric mass density. Assuming that this amount of air is accelerated to the same speed as the spacecraft, its momentum is $\rho Av^2\Delta t$. The momentum gained by the atmosphere per unit time, equivalent to that lost by the spacecraft per unit time, is ρAv^2 . This is the aerodynamic force acting on the spacecraft, a result which is surprisingly accurate (Withers 2013). Even with sophisticated numerical simulations, the aerodynamic force on a spacecraft is typically within a few tens of percent of ρAv^2 . Neglecting the effects of gravity on the spacecraft (mass m), which is reasonable in the initial stages of atmospheric entry, gives the drag equation.

$$m \frac{dv}{dt} = -\rho Av^2 \frac{C}{2} \quad (1)$$

The dimensionless coefficient C , which is close to 2, accounts for small deviations from the idealized situation outlined here.

Given knowledge of a spacecraft's entry trajectory, the profile of atmospheric density along this trajectory can be found using Equation 1. The trajectory is reconstructed using *in situ* measurements of acceleration during entry and the initial state of the spacecraft at the top of the atmosphere. Reliable density measurements are obtained over a wide vertical range. The upper boundary, which is generally at thermospheric altitudes, is set by instrumental sensitivity. The lower boundary, which is generally deep in the troposphere, is the altitude of parachute deployment. Spacecraft dynamics under a parachute are complex, which makes it difficult to determine atmospheric density from acceleration measurements once a parachute is deployed.

Atmospheric entry profiles at Mars have been acquired by Viking Landers 1 and 2, Pathfinder, Spirit, Opportunity, Phoenix, Curiosity, and InSight (Seiff & Kirk 1976; Magalhães et al. 1999; Withers & Smith 2006; Withers & Catling 2010; Holstein-Rathlou et al. 2016; Banfield et al. 2020). Typical vertical extent is 10–100 km. We analyze small-scale structure in all atmospheric profiles from the descent of these landers. The locations, seasons, and times of day of these entry profiles are listed in Table 2.

8. OBSERVATIONS OF SMALL-SCALE STRUCTURE IN THE MIDDLE ATMOSPHERE

8.1. Approach

We use a four-step procedure to characterize the waves present in the four occultation reanalysis profiles (two channels for each immersion and emersion) and the eight entry profiles. This procedure focuses on perturbations in the density profile, as density is the atmospheric property most closely connected to the flux (occultation) and acceleration (entry) measurements directly observed.

Our procedure is as follows.

(1) *Density excursion.* Following Person et al. (2008), we isolate density departures from an idealized, isothermal atmosphere. We fit observed number density (n) to the isothermal model

$$\bar{n} = n_0 e^{(z-z_0)/H}, \quad (2)$$

where n_0 is a reference density, z_0 is a reference altitude, and H is the pressure scale height. The density excursion is given n/\bar{n} .

(2) *High-pass filter.* The features of greatest interest are those of short vertical wavelength, not the larger-scale thermal tides. We therefore use a high-pass filter to isolate the shorter wavelength scales. Specifically, we employ the Savitzky-Golay filter, often called “savgol,” which fits a polynomial of order M to a window of size N at each point in the data (Savitzky & Golay 1964). In our experiments, $M = 2$ had the greatest success removing artifacts and values of N in the range [3, 40] km were explored. We calculate a savgol filter value (SG) for each density excursion and subtract it off, leaving behind an isolated waveform of interest.

492 In our experiments, any individual choice of window size N has certain limitations. For example,
493 a window size of 5 km will filter out most longer wavelengths, creating the perception that those
494 wavelengths are not present in the data. This is desirable in the case of thermal tides, which we
495 want to distinguish clearly from small-scale perturbations. But in identifying the relative strengths
496 of 5 and 10 km waves, for example, we do not wish for the user-defined filter window to significantly
497 impact our findings, which is why we perform many filterings.

498 (3) *Amplitude Spectrum.* We find the amplitudes of harmonic contributions present in each profile
499 from the Fourier transform of the filtered wave. As mentioned above, we choose to savgol filter each
500 profile at many different filter window sizes, each of which produces an amplitude spectrum. We
501 compiled the results of these spectra into contour plots, which show filter window versus wavelength.
502 The contour levels indicate amplitudes. The plots are shown in Section 8.2 and Figures 6 and 7.

503 As mentioned in Section 4, numerical inversion of an individual flux measurement in an occultation
504 light curve is highly dependent on the previous point. Therefore, inversion has the potential to create
505 waves out of smooth light curves with random noise. We tested this by using a control set of idealized,
506 isothermal light curves with the same noise profile as the real occultation data. We inverted and
507 processed these light curves and detected the distribution of peak amplitudes for each savgol filter
508 window used on the real data. The resulting distributions are skew-normal, and are used to calibrate
509 confidence intervals for the stellar occultation amplitude spectra shown in Section 8.2.

510 (4) *Amplitude Growth.* We look for wave amplitude variations that follow gravity wave theory
511 ([Mueller-Wodarg et al. 2008](#)) and compare with static stability.

512 Under stable atmospheric conditions, waves typically grow in amplitude as they propagate vertically
513 because the decreasing atmospheric density requires greater amplitude to satisfy conservation of
514 energy flux ([Holton 2013](#)). For each extracted wave form, we assessed the dependence of wave
515 amplitude on altitude by identifying the wave peaks and finding the corresponding peak-to-peak
516 amplitude values. We look for amplitude growth following the pattern $A \propto n^{-(1/2)}$ ([Mueller-Wodarg](#)
517 et al. 2008), where A is the filtered wave amplitude and n is number density.

518 Wave propagation is influenced by the atmospheric static stability. Static stability is defined as
 519 the difference between the dry adiabatic lapse rate Γ_d and the observed lapse rate Γ , which can be
 520 written

$$\Gamma_d - \Gamma = \frac{g}{c_p} + \frac{\partial T}{\partial z} \quad (3)$$

521 where c_p is the specific heat at constant pressure of the atmosphere ($850 \text{ J kg}^{-1} \text{ K}^{-1}$; Magalhães et al.
 522 (1999)), g is the gravitational acceleration, and T is temperature (Holton 2013). A value of static
 523 stability near or below zero indicates regions of the atmosphere where the observed adiabatic lapse
 524 rate exceeds the limit of convective stability. It is held that convection quickly reduces the lapse
 525 rate to restore equilibrium, meaning that wave transport is likely not stable in this region and wave
 526 breaking might occur. We compare wave activity to static stability for each of the profiles.

527 Wave activity is further illustrated if we represent the filtered density excursion by a simple model:

$$1 + c_1 n(z)^{-\frac{1}{2}} \sin \left[\left(\frac{2\pi z}{c_2} \right) - c_3 \right] \quad (4)$$

528 where c_1 , c_2 , and c_3 are parameters determined by approximately matching the model to the filtered
 529 density excursion. c_1 scales the width of the envelope of amplitude growth, c_2 is the wavelength,
 530 determined by the amplitude spectrum, and c_3 determines the phase of the sine curve to align with
 531 the observed wave.

532 8.2. Stellar Occultation Wave Results

533 Figures 6 and 7, each show two sets of four-panel plots, where a row of four subplots corresponds
 534 to a data source (e.g., emersion channel 2). There are two channels (2 and 3) and two areas of
 535 the planet probed (at immersion and emersion). The columns in these four-panel plots show, from
 536 left to right, density excursion, savgol filtered waves, peak-to-peak amplitude, and static stability.
 537 In the second column of these figures, we display the results of a 10 km savgol filter window, the
 538 reasoning for which is given below. A visual inspection of the third column in these figures leads to
 539 the conclusion that the emersion channel 2 data (Figure 6c) most closely follows the trend of wave

540 growth. Specifically, wave growth is consistent between 65 and 95 km, below which a pattern of
541 decreasing amplitude might indicate wave saturation or breaking. This interpretation of Figure 6c is
542 corroborated by Figure 6d, which shows a high static stability between 65 and 95 km, bookended by
543 low static stability.

544 The static stability of immersion profiles (Figures 7d and 7h) show some regions of high static
545 stability, but frequent dips toward zero support the finding that those waves do not indicate amplitude
546 growth. Despite this, Figures 7b and 7f do show narrow regions where waves are stable, even some
547 of particularly large amplitude.

548 As detailed in Section 8.1, Figure 8 shows the contour plot of amplitude spectra for every savgol
549 filter window of 3–40 km. Colored contours indicate amplitudes as a function of wavelength (y-
550 axis) for a given filter window (x-axis). The white contour lines indicate confidence intervals from
551 control data. We indicate amplitudes at each savgol window size that are confident to the 95% and
552 99.99% level based on the distribution of amplitude peaks from the control data. For instance, a 1%
553 amplitude wave is highly significant ($> 99.99\%$) when using a 10 km filter window. The same 1%
554 amplitude is not significant when using a 30 km filter window. This underscores the motivation of
555 using many filter windows.

556 Having both amplitudes and significances in Figure 8 enables us to hone in on the features of
557 greatest interest. The large, highly significant, yellow features in the upper right-hand corner of each
558 plot are the thermal tides. They are of much greater amplitude in the immersion data. Features
559 of wavelength 8–12 km appear in all four profiles at high confidence as well, with amplitudes in the
560 range of 1.4–3%. We also see features of wavelength 4–6 km with amplitudes in the range 0.5–1%.
561 These latter two groups of features are of greatest interest because they exhibit wavelengths and
562 amplitudes consistent with gravity wave features in the middle atmosphere of Mars.

563 In particular, the 4–6 km features would represent smaller wavelengths than have been detected
564 previously if confirmed. Because these features are best detected with a savgol filter window of 10
565 km, we used that particular window size in Figures 6 and 7. Prior works referenced in Section 2 also
566 chose to filter out perturbations with wavelengths longer than about 10 km. Tellmann et al. (2013b)

567 used a 10 km vertical wavelength filter to remove tidal modes and Wright (2012) performed a similar
568 filtering.

569 In Figure 9, we show the amplitude spectrum with the 10 km filter, essentially a cut at $x = 10$
570 km in Figure 8. All four profiles show 4–6 km wavelength modes with significance exceeding 95%
571 confidence, with two of them exceeding 99.99% confidence. Furthermore, the emersion channel 2
572 profile in Figure 8c is dominated by one wave mode more than any other, which is likely why that
573 profile has the clearest indication of wave amplitude growth in Figure 6c.

574 We fit the gravity wave model (Equation 4) to the filtered emersion channel 2 profile (Figure 6b),
575 finding the best fit with $c_1 = 2.3 \times 10^7 \text{ m}^{-\frac{3}{2}}$, $c_2 = 5.2 \text{ km}$, and $c_3 = 1.3 \text{ radians}$. Figure 10 shows the
576 model overplotted on the filtered profile. The model and observations agree well between 65 km and
577 95 km altitude, where the atmosphere is most stable for gravity wave propagation.

578 Overall, we find waves of wavelength 4–6 km and 8–12 km in the middle atmosphere of Mars from
579 stellar occultation profiles that are consistent with gravity wave activity.

580 8.3. *Entry Profile Wave Results*

581 We produced plots showing density excursion, savgol filtered waves, peak-to-peak amplitude, and
582 static stability for the entry profiles in the same manner as for the occultations. For the entry profiles
583 we display the results of the 20 km savgol filter window, the reasoning for which is offered below.

584 Figure 11a–d shows the Viking 1 entry results. Figure 11b indicates varied wave activity, which
585 in Figure 11c shows a limited agreement with the wave growth model below 60 km. Above 60 km
586 there is a narrow region of wave dissipation coinciding with static stability below zero in Figure 11d.
587 Above about 70 km, wave activity is again high and only shows potential dissipation above 100 km.
588 The generally low static stability in Figure 11d might limit wave growth.

589 Figure 11e–h shows the Viking 2 entry results. Figure 11f shows lots of wave activity but Figure
590 11g indicates it does not follow the theoretical wave growth pattern. Figure 11h indicates regions of
591 negative stability at 50 km and 100 km, but where stability is higher in the middle atmosphere, the
592 highest amplitude waves are found.

593 Figure 11i–l shows the Pathfinder entry results. Figure 11j shows a steady wave pattern throughout,
594 interrupted by two large wave trains between 60 and 95 km in altitude. Figure 11k indicates each
595 of these wave trains follows the predicted wave growth pattern before breaking at 80 and 95 km.
596 Figure 11l shows static stability is often low but does not dip below zero considerably in the middle
597 atmosphere, consistent with each wave train briefly growing.

598 Figure 11m–p shows the Spirit entry results. Figure 11n depicts a visibly growing wave structure,
599 which Figure 11o demonstrates follows the wave growth trend throughout the atmosphere. Figure
600 11p indicates high stability at all altitudes except those above 100 km, bolstering the case for a
601 propagating wave in this profile.

602 Figure 12a–d shows the Opportunity entry results. Figure 12b is not as clear as Figure 11n but
603 Figure 12c shows a global trend consistent with wave amplitude growth. Figure 12d indicates, as
604 with Spirit, that the atmosphere is statically stable at all altitudes but those above 100 km.

605 Figure 12e–h shows the Phoenix entry results. Figure 12g identifies that amplitude growth follows a
606 wave pattern from the bottom of the profile up to about 62 km, where the wave amplitude decreases.
607 Figure 12h shows static stability greater than zero for all altitudes below 80 km, indicating the
608 amplitude decrease at 65 km is more likely to be wave saturation or dissipation than breaking. The
609 difference between dissipation and breaking can be exemplified by comparing this figure to Figure
610 11k at 95 km.

611 Figure 12i–l shows the Curiosity entry results. Figure 12k shows a weak growth pattern up to about
612 60 km with another, briefer, wave growth pattern from 70 km to about 90 km. Figure 12l shows a
613 decrease in static stability below zero at about 63 km, which coincides with saturation in the lower
614 wave pattern. Static stability jumps up again above 80 km, coinciding with the upper wave pattern.

615 Figure 12m–p shows the InSight entry results. A starkly visible wave train in Figure 12n extends
616 from 60 km to 100 km at the top of the profile, with a maximum amplitude, as indicated in Figure
617 12o, at 75 km. Figure 12o indicates expected wave growth from the bottom of the profile up to about
618 75 km. Figure 12p shows static stability significantly greater than zero for the entirety of the profile,

dropping lowest at about 65 km, which might precipitate the wave train dissipation above 75 km.
Like Figure 12g, this pattern is more likely to be wave dissipation than breaking.

Figure 13 shows the amplitude spectra contour plots for the entry profiles in the same manner as Figure 8 for the occultations. Upon inspection of the contour plots, we see that the features of 20–30 km wavelength that only appear with larger filter windows are likely thermal tides. Regardless of their exact nature, they are not within the scope of this work and we therefore focus on the features of 9–14 km that appear with strong regularity. A 20 km filter window does a good job removing the large waves while keeping the 9–14 km features, which is our motivation for displaying the four-panel plots above with that filter.

Figure 14 shows the amplitude spectra of the entry profiles for the 20 km savgol filter window. Here we can see the 9–14 km features appear across all the profiles, ranging in amplitudes 0.8–2.6%. Some profiles, e.g., Spirit, show two-peaked features and others, e.g., Pathfinder, show single-peaked features.

8.4. Comparison of Primary Wave Findings

The wavelengths, peak amplitudes, and confidences of all waves identified in the amplitude spectrum contours (Figures 8 and 13) are given in Table 3. From the occultation profiles, wave species are included only if they exceeded the 95% confidence and have wavelengths between 3 and 20 km. From the entry profiles, wave species are included only if they exceed amplitude of 0.5% and have wavelengths between 3 and 20 km.

Figures 8 and 13 and Table 3 reveal common attributes between the occultation and entry profiles. Wavelengths in the range 9–14 km are detected across many profiles, with amplitudes predominantly 1%–2.5%. Gravity waves within this range of wavelengths are among the most common detected in the Martian atmosphere (Tellmann et al. 2013a; Siddle et al. 2019).

These results additionally reveal contrast between the occultation and entry profiles. Occultation profiles reveal waves of shorter wavelength (3–6 km) and entry profiles reveal waves of longer wavelength (16–20 km).

645 9. INTERPRETATION

646 Short-wavelength fluctuations comparable to those discussed in Section 8 have been seen throughout
 647 the Mars atmosphere by a variety of limb sounding instruments. They have generally been interpreted
 648 as gravity waves.

649 Numerous types of internal waves can exist in the atmosphere of Mars (Yigit & Medvedev 2015).
 650 We consider acoustic waves, internal gravity waves, inertia-gravity waves, Rossby waves, and tides.
 651 (Andrews et al. 1987; French & Gierasch 1974).

652 Acoustic waves satisfy $\omega \gg f$, where ω is the angular frequency of the wave, f is the Coriolis
 653 parameter, $f = 2\Omega|\sin\phi|$, Ω is the rotation rate of the planet, and ϕ is latitude. For the vertical
 654 wavelength of 3–6 km required by Section 8.2, their horizontal wavelength would be less than 10
 655 km, much shorter than the path length of starlight through the atmosphere of Mars. Such waves
 656 cannot be responsible for coherent vertical structure in the atmospheric profile obtained from a stellar
 657 occultation.

658 Internal gravity and inertia-gravity waves are similar. Both satisfy $f < \omega < N$, where N is the
 659 Brunt-Väisälä or buoyancy frequency. This is defined as:

$$N^2 = \frac{-g}{\rho_0} \frac{\partial \rho}{\partial z}. \quad (5)$$

660 For the vertical wavelength of 3–6 km required by Section 8.2, their horizontal wavelength is compa-
 661 rable to the path length of starlight through the atmosphere of Mars. Such waves may be responsible
 662 for coherent vertical structure in the atmospheric profile obtained from a stellar occultation.

663 Rossby waves satisfy $\omega \ll f$. For the vertical wavelength of 3–6 km required by Section 8.2,
 664 they have horizontal wavelengths many times greater than the path length of starlight through the
 665 atmosphere of Mars. Such waves may be responsible for coherent vertical structure in the atmospheric
 666 profile obtained from a stellar occultation.

667 Tidal modes with the vertical wavelength of 3–6 km required by Section 8 do not propagate effi-
 668 ciently to the middle atmosphere of Mars (Withers et al. 2003a). Such waves cannot be responsible
 669 for coherent vertical structure in the atmospheric profile obtained from a stellar occultation.

We exclude Rossby waves from consideration, despite their long horizontal wavelength, because general circulation models indicate that Rossby waves on Mars would be confined to the very lowest regions of the atmosphere due to topographic forcing and dissipative effects (Fazel-Rastgar 2019). That leaves internal gravity waves and inertia-gravity waves as possible causes of the observed short-wavelength fluctuations.

Internal gravity waves are instances of inertia-gravity waves in which the effects of planetary rotation are small. This is equivalent to the Coriolis parameter in the dispersion relation being negligible (Andrews et al. 1987; French & Gierasch 1974; Yiğit & Medvedev 2015). For the short vertical wavelength relevant here, effects of planetary rotation are negligible.

Furthermore, numerical models of the mesosphere of Mars can reproduce gravity waves with features similar to those reported here. Spiga et al. (2012b) produced \sim 10 km vertical wavelength gravity waves throughout the atmosphere (10 - 110 km altitude). Parish et al. (2009) produced gravity waves with 12 km vertical wavelength at about 25 km altitude.

We therefore concur with the widespread conclusion that short-wavelength fluctuations in Mars atmospheric profiles are caused by gravity waves. The species of 3–14 km wavelength that dominate detections in Table 3 align with previous detections and theoretical studies. The few detections of perturbations with longer wavelengths might be attributable to other sources. Regardless, the overlap in detections between the stellar occultations and spacecraft entry profiles corroborates the interpretation of these perturbations as caused by gravity waves.

10. DISCUSSION

In section 1, we raised questions about gravity waves in the middle Martian atmosphere, the answers to which would significantly aid efforts to understand the critical middle atmospheric region and draw connections between upper and lower atmospheric dynamics. Here we answer these questions based on the findings in this work.

What are the characteristic vertical wavelengths of gravity waves in the middle atmosphere?

From re-analyzing of the 1976 Mars occultation of ϵ Geminorum and analyzing the entry profiles of eight spacecraft, we find gravity waves predominantly with vertical wavelengths 3–14 km. See Table 3 for the breakdown of which wavelengths were detected from which data source.

What are the amplitudes of gravity waves in the middle atmosphere?

From producing amplitude spectra, we find amplitudes of dominant wavelengths in the middle atmosphere mostly fall in the range 0.8%–2.5%. A close inspection of Figures 6, 7, 11 and 12 reveals that in regions of the atmosphere most conducive to wave growth (positive static stability), amplitudes grow as large as 5% before saturating, dissipating, or breaking. See Table 3 for the summary of wave amplitudes from each data source.

What regions in the Martian atmosphere are most conducive to gravity wave propagation? How does gravity wave amplitude change with altitude in the middle atmosphere?

Within both the entry profiles and the occultation profiles, we can identify regions of the middle atmosphere more and less conducive to wave propagation. For example, Figure 6a–d (channel 2 occultation emersion) indicates wave growth from 65 km to 90 km, where wave amplitude grows from 0.2% to 1%. Static stability remains far above zero for that altitude range. The Spirit results in Figure 11m–p show a growing wave from 60 km to 110 km, with amplitude growing from 1% to 5%. Static stability is far above zero for all but the highest altitudes in that range.

Other entry profiles indicate a different pattern of atmospheric stability. For example, the Phoenix profile in Figure 12e–h indicates significant wave growth from 30 km to 62 km, with amplitude growing from 1% to 5%, but above 62 km, no clear wave growth is detected. Static stability corroborates this finding. In this case, with notable similarities to Pathfinder (Figure 11i–l) and InSight (Figure 12m–p), we see wave dissipation in an atmospheric region less conducive to wave propagation. In the case of InSight, this dissipation occurs at much higher altitudes, where effects such as molecular viscosity and radiative damping have been shown to have significant effect on wave patterns (Eckermann et al. 2011). The immersion occultation profiles show similar characteristics, with narrow vertical bands of stability, flanked by wave saturation and/or breaking.

We see that in regions of greater-than-zero stability, gravity wave amplitude follows the growth trend $A \propto n^{-1/2}$. In regions where stability barely dips below zero, e.g., Curiosity (Figure 12i–l) at 62 km, wave growth patterns are disrupted. Moreover, in regions where static stability remains close to or repeatedly dips below zero, e.g., Viking 2 and Pathfinder (Figures 11e–h and 11i–l), no global wave growth patterns can be established and wave growth is frequently interrupted. Both Viking profiles are curious in this manner because both amplitude spectra (Figures 14a and 14b) indicate a clear presence of waves that aligns with a visual inspection of the extracted waveforms (Figures 11b and 11f), but no global wave growth pattern is present (Figures 11c and 11g). The immersion channel 2 profile in Figure 7e–h has a region of stable wave growth following the amplitude trend only above 80 km.

This idealized wave growth pattern can only be expected for a quiescent atmosphere with positive static stability. Where these conditions are met globally, e.g., occultation emersion (Figure 6) and Spirit (Figure 11m–p), we can expect gravity wave propagation throughout. Profiles in which these conditions are met only in narrow vertical ranges, e.g., occultation immersion (Figure 7), Phoenix (Figure 12e–h), and Pathfinder 11i–l, or not at all, e.g., Viking 2 (Figure 11e–h), do not by default indicate a lack of gravity wave activity.

What seasonal, diurnal, and latitudinal patterns in gravity wave activity exist?

We explored amplitude and wavelength patterns with season, time of day, and latitude for all occultation and entry profiles and found no identifiable trends. We therefore reiterate the long-held finding that gravity wave activity is nearly universal on Mars.

11. CONCLUSIONS

Gravity waves are ubiquitous in the atmosphere of Mars. They have been studied extensively in the lower and upper atmosphere, but not in the middle atmosphere. Suitable atmospheric profiles that sample the middle atmosphere with good vertical resolution have been obtained by a stellar occultation from 1976 that yielded immersion and emersion profiles on opposite sides of the planet, and eight profiles measured during atmospheric entry by landers and rovers.

This analysis of those observations has characterized the wavelengths and amplitudes of gravity waves in the middle atmosphere. Predominant wavelengths are 3–14 km and amplitudes are generally 0.8%–2.5%. Where static stability is large and positive, gravity waves grow efficiently. For the entry of the Spirit rover, for example, gravity wave amplitude grows from 1% at 60 km to 5% at 110 km in accordance with the dependence on atmospheric density expected from idealized theoretical calculations. In other instances, static stability is not large and positive over a wide altitude range, and gravity wave amplitudes do not behave as neatly.

These observations of gravity waves in the middle atmosphere of Mars can be used to test gravity wave parameterizations in large-scale general circulation models and to investigate predictions for how gravity wave propagation and dissipation influence the circulation and thermal structure of the middle and upper atmosphere.

For example, they offer the detailed wave spectra in the middle Martian atmosphere required by the general circulation model of Medvedev et al. (2011). Moreover, our results may serve as benchmarks for the missing middle atmosphere inputs for a model developed by Kuroda et al. (2015), which incorporated small-scale gravity waves and used radio occultation observations (Creasey et al. 2006a) to benchmark results in the lower atmosphere (10–30 km), but could not constrain results higher up.

These modeling efforts among others (Yiğit et al. 2008; Eckermann et al. 2011; Medvedev & Yiğit 2012; Lott et al. 2012; Yiğit et al. 2015; England et al. 2017; Gilli et al. 2020) are aided by our new analysis and characterization of the middle atmosphere gravity waves reported here.

ACKNOWLEDGMENTS

We acknowledge the work of the late Prof. James Elliot in taking these observations and performing the original analysis. The authors thank the two anonymous reviewers for their suggestions that significantly improved the quality of the manuscript.

APPENDIX

769 A. INVERSION PROCESS

770 Inversion of stellar occultation observations requires a number of assumptions, the most significant
771 of which are as follows.

- 772 1. Atmospheric variation is a function of altitude only, implying uniformity across the planet at
773 each altitude level.
- 774 2. Atmospheric composition is uniform.
- 775 3. The atmosphere is in hydrostatic equilibrium.
- 776 4. Extinction is negligible compared to refraction.
- 777 5. Bending angles due to refraction are small.
- 778 6. Planetary altitudes probed in immersion and emersion vary monotonically, *i.e.*, there is no ray
779 crossing.
- 780 7. The Martian atmosphere is clear during these observation, *i.e.*, without dust or haze. (See
781 Section 5.2.)

782 On small bodies with atmospheres significantly less than the terrestrial atmosphere, these assump-
783 tions hold reasonably well. The original work of Elliot et al. (1977b) had one additional assumption,
784 no longer required here, that the atmospheric scale height H is much less than the radius of Mars
785 (Wasserman & Veverka 1973; French et al. 1978).

786 Figure 15 shows the geometry of atmospheric refraction that is solved by inversion. Figure 16 is
787 a flowchart showing the steps of inversion from the normalized flux light curve $\phi(t)$ to atmospheric
788 properties. The other starting parameter is $y(t)$, where y is the distance of the observer relative to a
789 reference point (usually defined at some arbitrary time before occultation). Values of y are calculated
790 from the impact parameter (22.12 ± 0.38 km) and event velocity (21.9 km/s).

791 Given $y(t)$ and $\phi(t)$ it is possible to calculate the flux as a position series $\phi(y)$. The distance
792 from the center of the occulting body corresponding to each flux measurement $r(y)$ is calculated

from y values given the distance between the observer and occulting body D , which is determined by ephemerides of Mars provided by JPL HORIZONS (<http://ssd.jpl.nasa.gov/?horizons>). $r(y)$ is solved using

$$r(y) = \left\{ y^2 + 2 \int_y^\infty [1 - \phi(y')] y' dy' \right\}^{1/2} \quad (\text{A1})$$

The bending angle $\theta(r)$, shown in Figure 15 is determined using $r(y)$ and D by assuming the small angle approximation:

$$\theta(r) = \frac{y(r)}{D} \quad (\text{A2})$$

$\theta(r)$ is related to atmospheric index of refraction $N(r)$ by the equation

$$\theta(r) = \int_{-\infty}^\infty \frac{r}{r'} \frac{d}{dr'} \ln N(r') dx \quad (\text{A3})$$

where x is defined by the geometry of Figure 15 as $x^2 = r'^2 - r^2$. r' is a variable of integration that iterates between 0 and r for each atmospheric shell of radius r . Refractivity $\nu(r)$ is preferred to index of refraction $N(r)$ and is related by

$$N(r) = 1 + \nu(r) \quad (\text{A4})$$

Equation A3 can be rearranged to solve for $N(r)$ by using an Abel transform (Abel 1826), which gives, using Equation A4

$$\nu(r) = -\frac{1}{\pi} \int_r^\infty \frac{\theta(r')}{\sqrt{r'^2 - r^2}} dr' \quad (\text{A5})$$

invoking the assumption $\nu \ll 1$. This is the critical step of inversion that amounts to “unpeeling” the atmosphere to determine the effect of the gas at each layer on the starlight passing through.

Number density $n(r)$ can be calculated from refractivity by the relation

$$n(r) = L \frac{\nu(r)}{\nu_{STP}} \quad (\text{A6})$$

where L is Loschmidt's number and ν_{STP} is a reference value assumed constant by the assumption of a homogenous atmosphere. The equation of hydrostatic equilibrium and ideal gas law close the system to solve for pressure $p(r)$, temperature $T(r)$ and scale height $H(r)$. The temperature-radius and pressure-radius results can be used to produce a temperature-pressure profile $T(p)$, which removes the sensitivity to the geometrical solution from model fitting.

The integrals in Equations A1, A3, and A5 are mathematically accurate but idealized because we cannot integrate to infinity, which is why boundary conditions from model fitting are so important. The numerical form of these integrals shown in [Elliot, Person, & Qu \(2003\)](#) combines the results of model fitting and uses discrete sums.

Uncertainties reported from the model fitting routine are used as the starting point of covariance matrices calculated for each inversion step. The final reported uncertainties are highly sensitive to the model fit parameters because of the high correlation between successive inversion points. In the original procedure from [Elliot, Person, & Qu \(2003\)](#), the model fit is only carried out to the top portion of the light curve, before inversion begins. We modified that procedure to fit the entire light curve and then begin inversion as high up as possible to further minimize uncertainties.

Many of the inversion steps remain the same in the [Elliot, Person, & Qu \(2003\)](#) approach as that of [French et al. \(1978\)](#), with a couple key improvements. (1) Inversion is adapted for high performance computing and can process high resolution light curves. (2) Error propagation is done in a mathematically sound manner instead of the estimates used in the original work. For details of the error analysis, the reader is referred to Section 4 of [Elliot, Person, & Qu \(2003\)](#).

REFERENCES

- 827 Abel, N. H. 1826, *Journal für die reine und* 858 Elliot, J. L., French, R. G., Dunham, E., et al.
828 *angewandte Mathematik*, 1, 153 859 1977a, *Science*, 195, 485
829 Ando, H., Imamura, T., & Tsuda, T. 2012, *J.* 860 —. 1977b, *ApJ*, 217, 661
830 *Atmos. Sci.*, 69, 2906 861 Elliot, J. L., Person, M. J., & Qu, S. 2003, *AJ*,
831 Andrews, D. G., Leovy, C. B., & Holton, J. R. 862 126, 1041
832 1987, *Middle atmosphere dynamics* (Academic 863 Elliot, J. L., & Young, L. A. 1992, *AJ*, 103, 991
833 press) 864 England, S. L., Liu, G., Yiğit, E., et al. 2017, *J.*
834 Banfield, D., Spiga, A., Newman, C., et al. 2020, 865 *Geophys. Res.*, 122, 2310
835 *Nature Geoscience*, 13, 190 866 Fazel-Rastgar, F. 2019, *Ap&SS*, 364, 54
836 Barnes, J. R., Haberle, R. M., Wilson, R. J., et al. 867 Feofilov, A. G., Kuteпов, А. А., Rezac, L., &
837 2017, in *The atmosphere and climate of Mars*, 868 Smith, M. D. 2012, *Icarus*, 221, 949
838 ed. R. M. Haberle, R. T. Clancy, F. Forget, 869 Forget, F., Montmessin, F., Bertaux, J., et al.
839 M. D. Smith, & R. W. Zurek, 202–228 870 2009, *J. Geophys. Res.*, 114, E01004,
840 Baum, W. A., & Code, A. D. 1953, *AJ*, 58, 108 871 10.1029/2008JE003086
841 Bosh, A. S., Person, M. J., Levine, S. E., et al. 872 French, R. G., & Elliot, J. L. 1979, *Astrophys. J.*,
842 2015, *Icarus*, 246, 237 873 229, 828
843 Chamberlain, D., & Elliot, J. 1997, *PASP*, 109, 874 French, R. G., Elliot, J. L., & Gierasch, P. J.
844 1170 875 1978, *Icarus*, 33, 186
845 Clancy, R. T., Sandor, B. J., Wolff, M. J., et al. 876 French, R. G., & Gierasch, P. J. 1974, *Journal of*
846 2000, *J. Geophys. Res.*, 105, 9553 877 *Atmospheric Sciences*, 31, 1707
847 Creasey, J. E., Forbes, J. M., & Hinson, D. P. 878 French, R. G., & Taylor, G. E. 1981, *Icarus*, 45,
848 2006a, *Geophys. Res. Lett.*, 33, L01803 879 577
849 Creasey, J. E., Forbes, J. M., & Keating, G. M. 880 Fritts, D. C., & Alexander, M. J. 2003, *Rev.*
850 2006b, *Geophys. Res. Lett.*, 33, L22814, 881 *Geophys.*, 41, 1003
851 10.1029/2006GL027583 882 Fritts, D. C., Wang, L., & Tolson, R. H. 2006, *J.*
852 Eckermann, S. D., Ma, J., & Zhu, X. 2011, *Icarus* 883 *Geophys. Res.*, 111, A12304,
853 211, 429 884 10.1029/2006JA011897
854 Elliot, J., & Olkin, C. 1996, *Annual Review of* 885 Gilli, G., Forget, F., Spiga, A., et al. 2020, *J.*
855 *Earth and Planetary Sciences*, 24, 89 886 *Geophys. Res.*, 10.1029/2018JE005873
856 Elliot, J. L., Dunham, E., & Church, C. 1976, 887 Gröller, H., Montmessin, F., Yelle, R. V., et al.
857 *S&T*, 52, 23 888 2018, *J. Geophys. Res.*, 123, 1449

- 889 Gubenko, V. N., Kirillovich, I. A., & Pavelyev, 920 Montabone, L., Forget, F., Millour, E., et al. 2015,
890 A. G. 2015, *Cosmic Research*, 53, 133 921 *Icarus*, 251, 65
- 891 Heavens, N. G., Kass, D. M., Kleinböhl, A., & 922 Montmessin, F., Bertaux, J.-L., Quémerais, E.,
892 Schofield, J. T. 2020, *Icarus*, 341, 113630 923 et al. 2006, *Icarus*, 183, 403
- 893 Holstein-Rathlou, C., Maue, A., & Withers, P. 924 Mueller-Wodarg, I. C. F., Strobel, D. F., Moses,
894 2016, *Planet. Space Sci.*, 120, 15 925 J. I., et al. 2008, *SSRv*, 139, 191
- 895 Holton, J. R. 2013, An introduction to dynamic 926 Parish, H. F., Schubert, G., Hickey, M. P., &
896 meteorology, fifth edition.. edn. (Amsterdam: 927 Walterscheid, R. L. 2009, *Icarus*, 203, 28
897 Elsevier : Academic Press) 928 Pasachoff, J. M., Person, M. J., Bosh, A. S., et al.
898 Houghton, J. 2002, The physics of atmospheres 929 2016, *AJ*, 151, 97
- 899 (Cambridge University Press) 930 Person, M. J., Elliot, J. L., Gulbis, A. A. S., et al.
900 Hubbard, W. B. 1982, *Adv. Space Res.*, 2, 103 931 2008, *AJ*, 136, 1510
- 901 Keenan, P. C., & McNeil, R. C. 1989, *ApJS*, 71, 932 Person, M. J., Dunham, E. W., Bosh, A. S., et al.
902 245 933 2013, *AJ*, 146, 83
- 903 Kieffer, H. H., Jakosky, B. M., Snyder, C. W., & 934 Person, M. J., Bosh, A. S., Zuluaga, C. A., et al.
904 Matthews, M. S. 1992, Mars 935 2019, *Icarus*, 113572
- 905 Kuroda, T., Medvedev, A. S., Yiğit, E., & 936 Quémerais, E., Bertaux, J.-L., Koralev, O., et al.
906 Hartogh, P. 2015, *Geophys. Res. Lett.*, 42, 9213 937 2006, *J. Geophys. Res.*, 111, E09S04,
907 Lemoine, F. G., Smith, D. E., Rowlands, D. D., 938 10.1029/2005JE002604
- 908 et al. 2001, *J. Geophys. Res.*, 106, 23359 939 Savitzky, A., & Golay, M. J. E. 1964, *Analytical
909 Lott, F., Guez, L., & Maury, P. 2012, 940 Chemistry*, 36, 1627
- 910 *Geophys. Res. Lett.*, 39, L06807 941 Seiff, A., & Kirk, D. B. 1976, *Science*, 194, 1300
- 911 Magalhães, J. A., Schofield, J. T., & Seiff, A. 942 Siddle, A. G., Mueller-Wodarg, I. C. F., Stone,
912 1999, *J. Geophys. Res.*, 104, 8943 943 S. W., & Yelle, R. V. 2019, *Icarus*, 333, 12
- 913 Medvedev, A. S., & Yiğit, E. 2012, 944 Smith, M. D., Bouger, S. W., Encrenaz, T.,
914 *Geophys. Res. Lett.*, 39, L05201 945 Forget, F., & Kleinböhl, A. 2017, in *The
915 Medvedev, A. S., Yiğit, E., Hartogh, P., & Becker 947 atmosphere and climate of Mars*, ed. R. M.,
916 E. 2011, *Journal of Geophysical Research* 948 Haberle, R. T. Clancy, F. Forget, M. D. Smith,
917 (Planets), 116, E10004 949 & R. W. Zurek, 20–41
- 918 Millour, E., Forget, F., Spiga, A., et al. 2019, in 950 Smith, M. D., Pearl, J. C., Conrath, B. J., &
919 *Geophysical Research Abstracts*, Vol. 21 951 Christensen, P. R. 2001, *J. Geophys. Res.*, 106,
951 23929

- 952 Spiga, A., González-Galindo, F., López-Valverde, 970
 953 M. Á., & Forget, F. 2012a, *Geophys. Res. Lett.*, 971
 954 39, L02201 972
 955 —. 2012b, *Geophys. Res. Lett.*, 39, L02201 973
 956 Tellmann, S., Pätzold, M., Häusler, B., Hinson, 974
 957 D. P., & Tyler, G. L. 2013a, *J. Geophys. Res.*, 975
 958 118, 306 976
 959 Tellmann, S., Pätzold, M., Häusler, B., Hinson, 977
 960 D. P., & Tyler, G. L. 2013b, *Journal of 978
 961 Geophysical Research (Planets)*, 118, 306 979
 962 Terada, N., Leblanc, F., Nakagawa, H., et al. 980
 963 2017, *J. Geophys. Res.*, 122, 2374 981
 964 Vals, M., Spiga, A., Forget, F., et al. 2019, *Planet 982
 965 Space Sci.*, 178, 104708 983
 966 Wasserman, L. H., & Veverka, J. 1973, *Icarus*, 20, 985
 967 322 986
 968 Withers, P. 2006, *Geophys. Res. Lett.*, 33, L02201 987
 969 —. 2013, *American Journal of Physics*, 81, 565 988
 Withers, P., Bouger, S. W., & Keating, G. M.
 2003a, *Icarus*, 164, 14
 Withers, P., & Catling, D. C. 2010, *Geophys. Res. Lett.*, 37, L24204, 10.1029/2010GL045382
 Withers, P., Pratt, R., Bertaux, J.-L., & Montmessin, F. 2011, *J. Geophys. Res.*, 116, E11005, 10.1029/2011JE003847
 Withers, P., & Smith, M. D. 2006, *Icarus*, 185, 133
 Withers, P., Towner, M. C., Hathi, B., & Zarnecki, J. C. 2003b, *Planet. Space Sci.*, 51, 541
 Wright, C. J. 2012, *Icarus*, 219, 274
 Yiğit, E., Aylward, A. D., & Medvedev, A. S. 2008, *Journal of Geophysical Research: Atmospheres*, 113
 Yiğit, E., & Medvedev, A. S. 2015, *Adv. Space Res.*, 55, 983
 Yiğit, E., England, S. L., Liu, G., et al. 2015, *Geophys. Res. Lett.*, 42, 8993
 Young, A. T. 1967, *AJ*, 72, 747

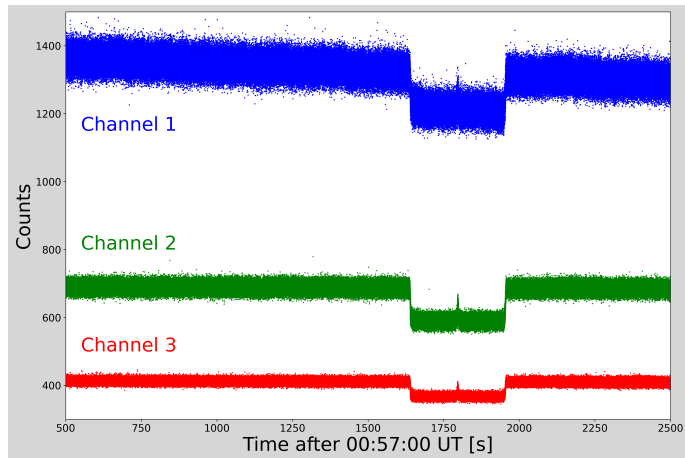


Figure 1. Raw data obtained from data storage device. Original resolution of 4 ms is plotted versus arbitrary electron counts. The upper baseline in Channel 1 has a clear negative trend that was fit to a line and corrected. Similar corrections were performed on the other channels.

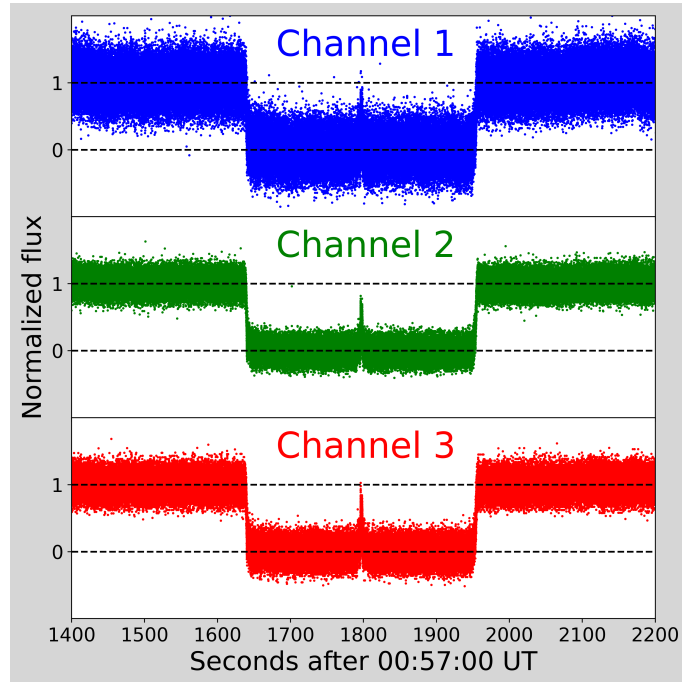


Figure 2. Normalized light curves of all three channels. Flux level is set to 1.0 at the upper baseline and 0.0 at the lower baseline, approximating no residual refraction around the limb away from immersion, emersion, and the central flash. The central flash in all three channels has two unequal peaks, not visible at this scale.

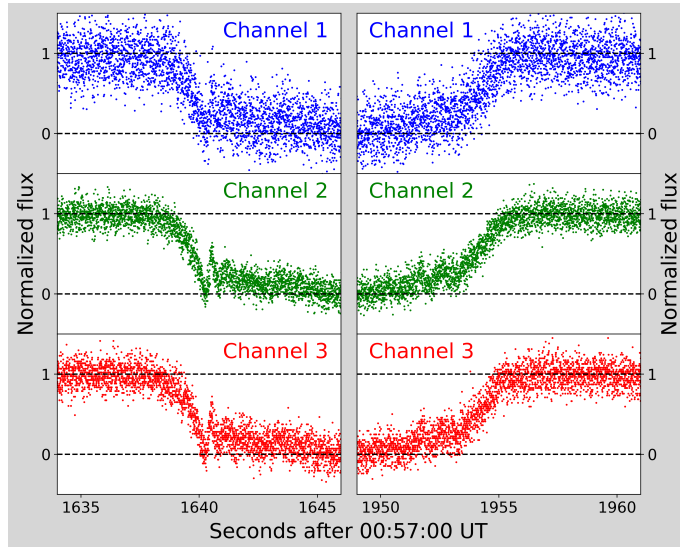


Figure 3. As in Figure 2, zoomed in on immersion and emersion. Here it is possible to see that channel 1 has much lower signal-to-noise than channels 2 and 3. Features of note include the prominent spikes and asymmetry of the profiles.

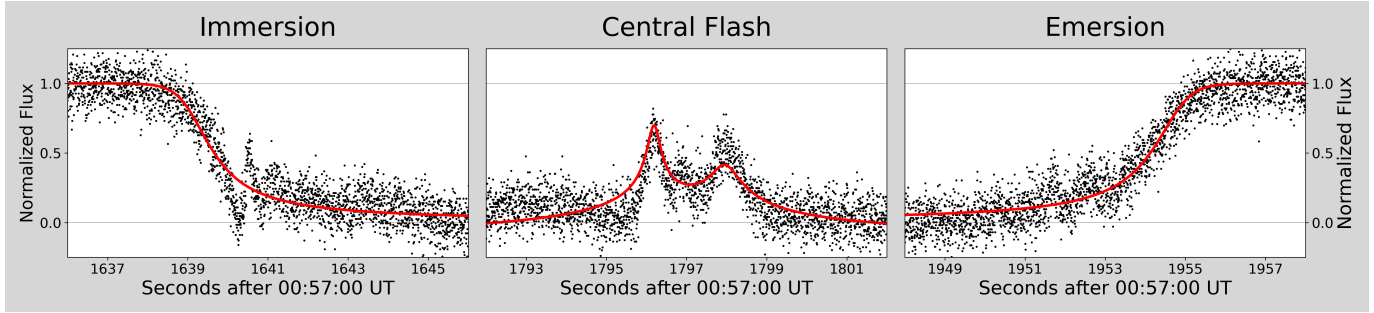


Figure 4. Isothermal model fits to immersion, central flash, and emersion curves following the Elliot & Young (1992) models. These model fits were used to set the upper boundary conditions at the start of inversion at 0.9 flux. The central flash fit was used to solve the event geometry for the impact parameter.

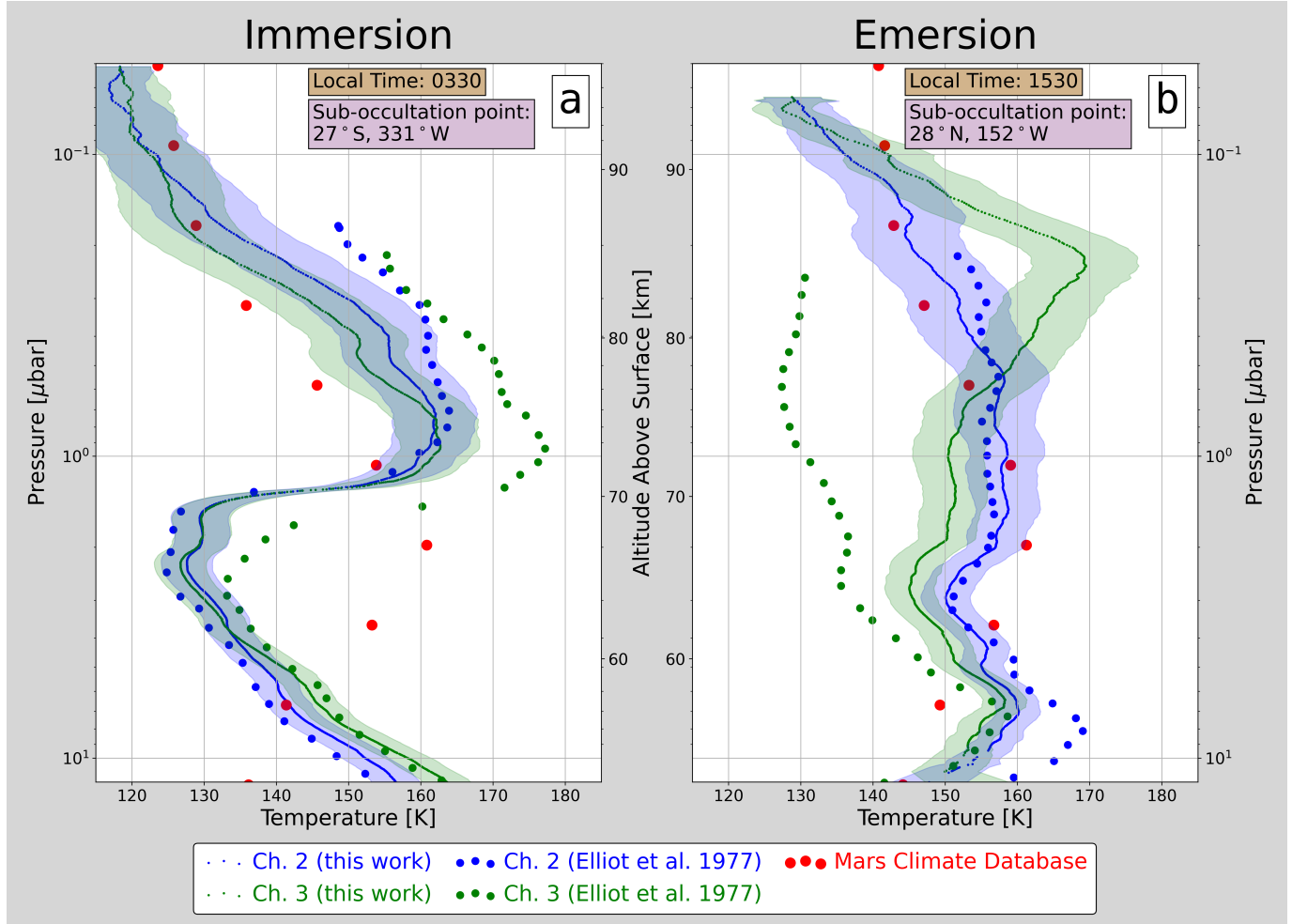


Figure 5. Temperature profiles of the middle Martian atmosphere. Reanalysis results in full resolution are compared to the original profiles of Elliot et al. (1977b) as well as the Mars Climate Database (MCD). The local Martian time of each profile and the surface sub-occultation point are indicated. The shaded regions represent uncertainty in temperature shifts of the entire profile because adjacent inversion results are highly correlated. The pressure scale is exact for all data being compared, but the altitude scale is approximate (See Section 6.1). The discrepancy between the MCD and occultation profiles below about $1 \mu\text{bar}$ can be attributed to differences in peak altitude and the lower vertical resolution of the MCD.

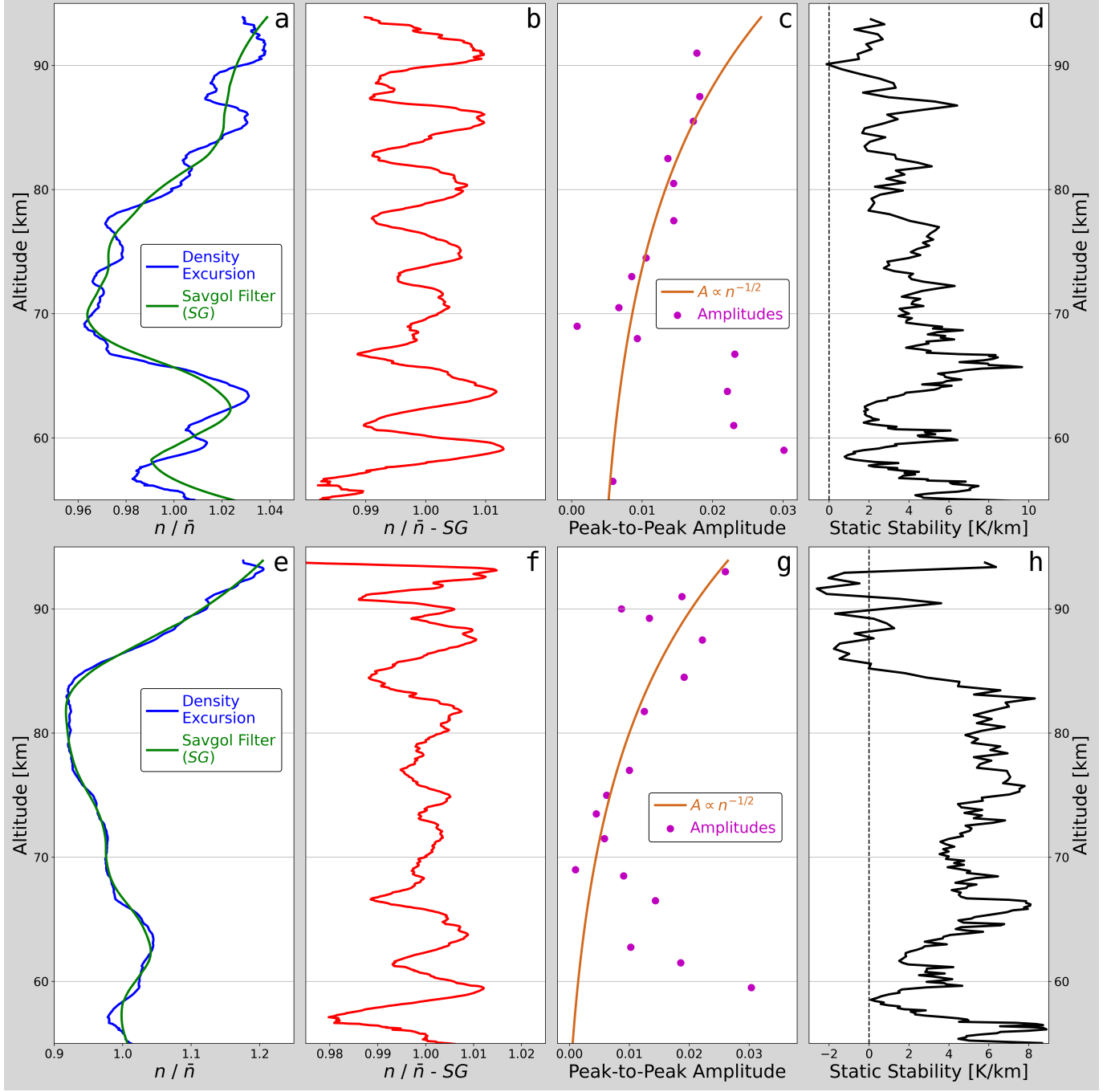


Figure 6. Occultation emersion channel 2 (a–d) and channel 3 (e–h). a, e. Density excursion (blue) resulting from dividing the density profile (n) by the exponential atmospheric model (\bar{n}). Small-scale waves and large waves (thermal tides) are superimposed, which motivated using the savgol filter (SG ; green) to isolate just the small-scale waves. b, f. The extracted small-scale wave, resulting from subtracting the savgol filter with 10 km filter window from the density excursion. c, g. Peak-to-peak amplitudes of the extracted wave (magenta). A model of gravity wave amplitude growth (Mueller-Wodarg et al. 2008) is overlaid (orange) to fit the amplitudes above 68 km altitude. d, h. Static stability determined by Equation 3. Altitudes where static stability decrease below or near zero, such as around 58 km and 90 km in panel d, indicate regions of the atmosphere that may have wave breaking.

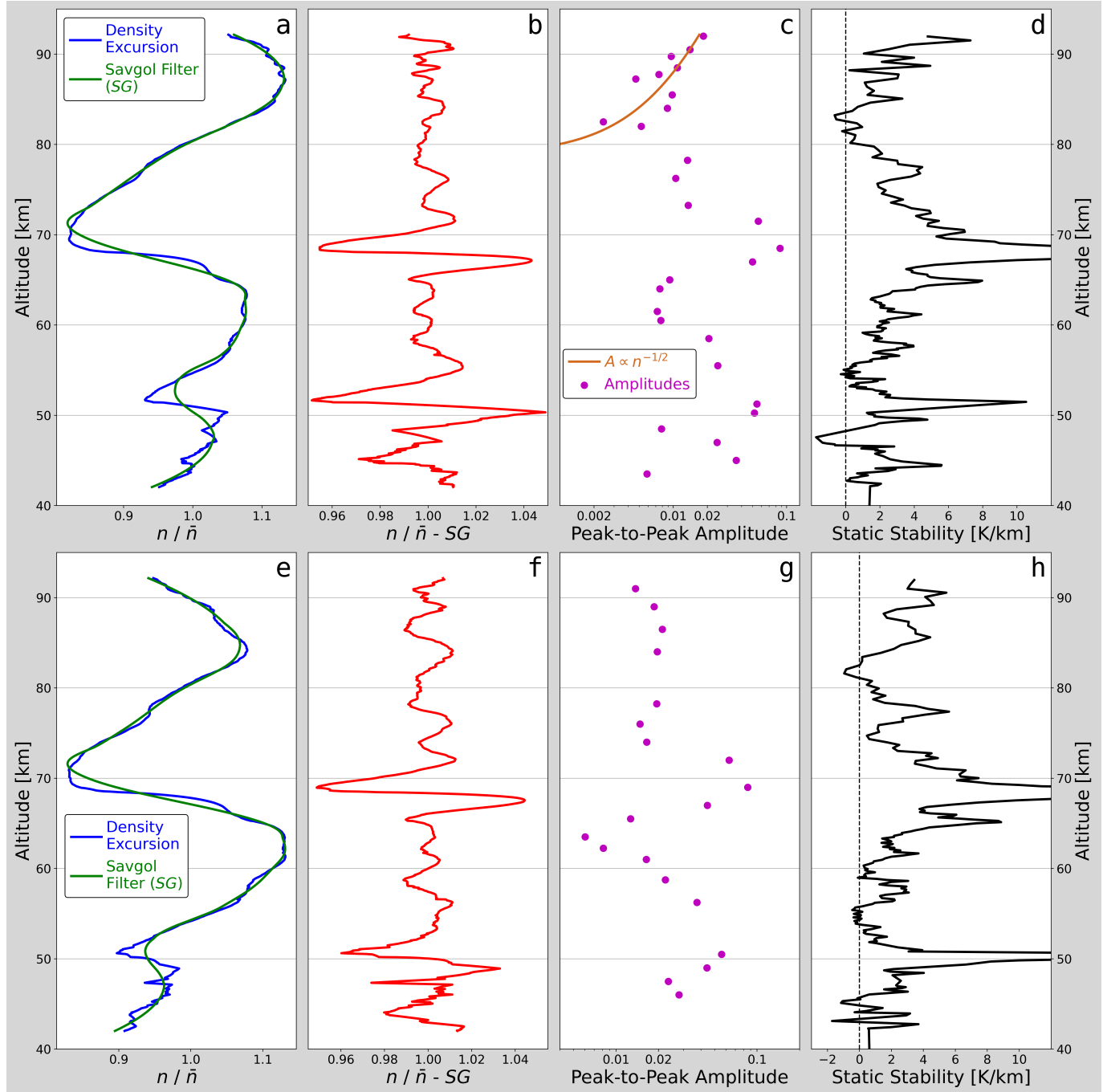


Figure 7. Occultation immersion channel 2 (a–d) and channel 3 (e–h) as in Figure 6.

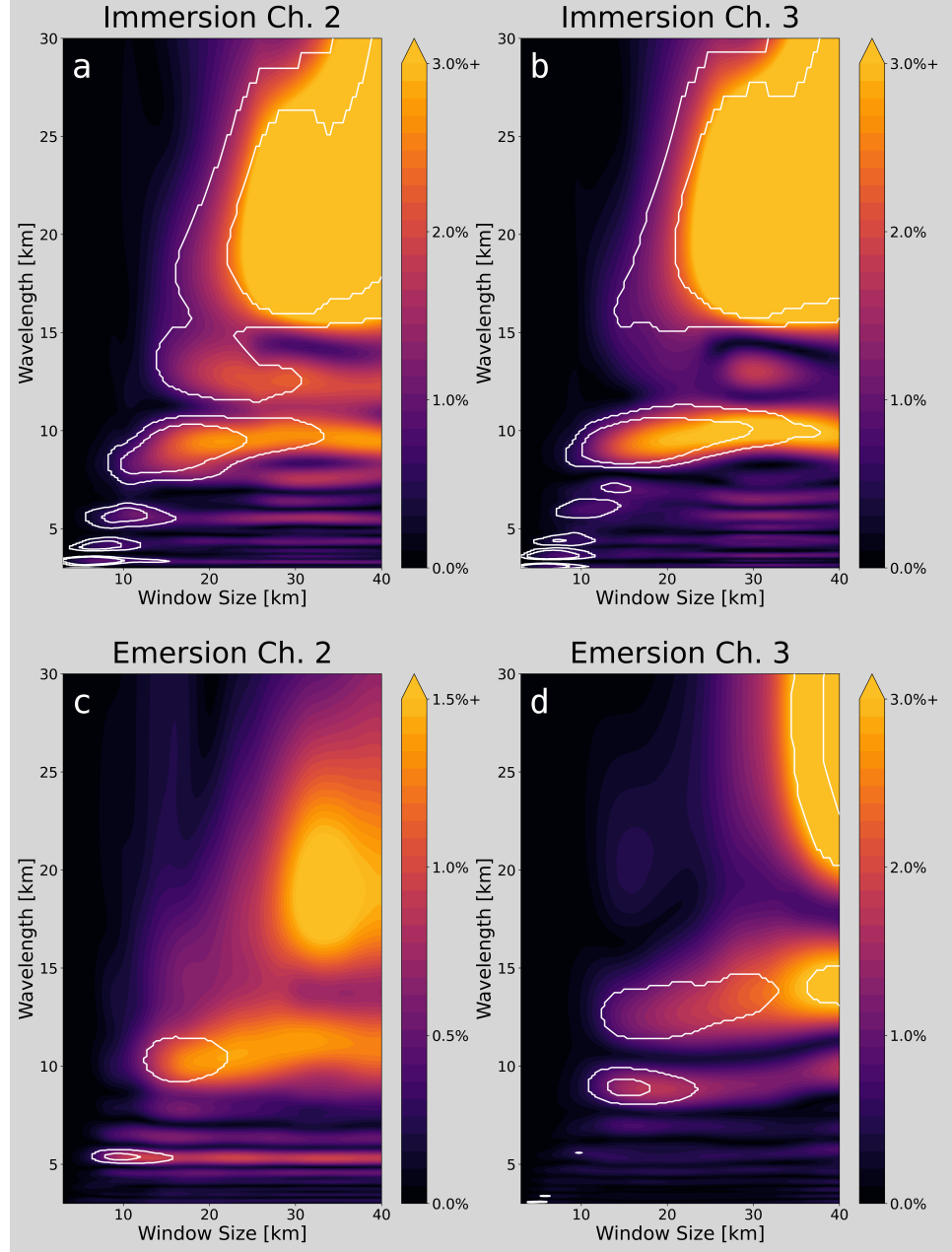


Figure 8. Amplitude spectra of all four occultation profiles represented as a contour plot. The x-axis is savgol filter window size, and y-axis is vertical wavelength of modes in the sample. The colored contour levels are wave amplitudes. The white contour lines indicate confidence intervals of the detected amplitudes, determined from a control test (see Section 8.1). The outer line is a 95% confidence and the inner line is 99.99% confidence.

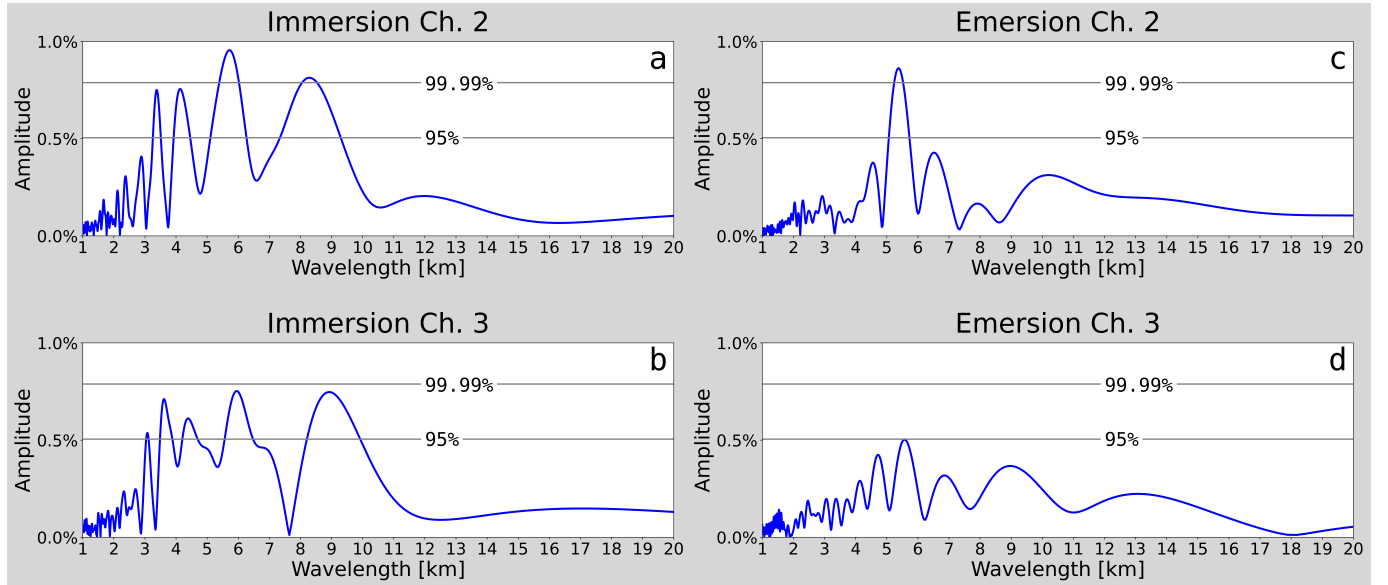


Figure 9. Amplitude spectra for occultation profiles with a savgol filter window of 10 km. Confidence intervals of 95% and 99.99% are indicated. Each spectrum is a slice through the corresponding two-dimensional panel in Figure 8 at a window size of 10 km.

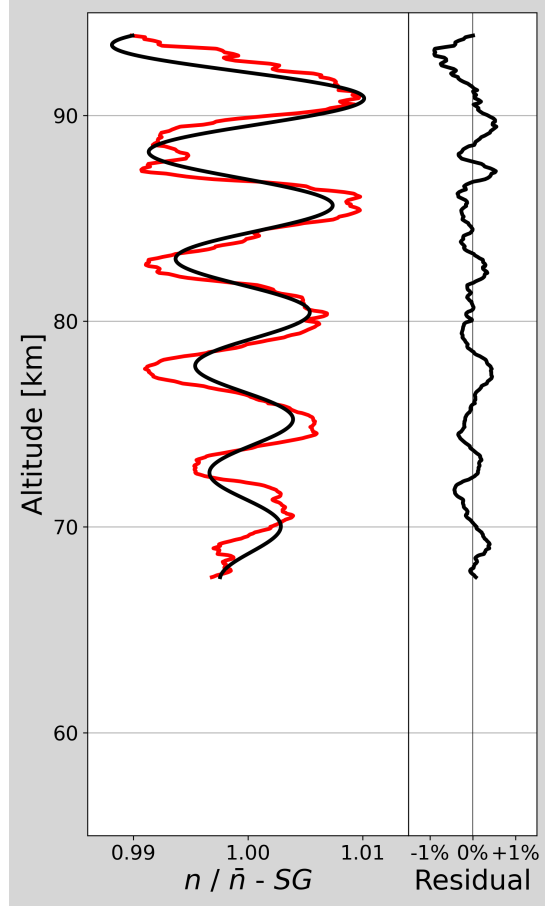


Figure 10. Extracted wave in Figure 6b (red) overlaid with the gravity model in Equation 4 (black). Model parameters were tuned by eye. Residuals are computed *data minus model* and are given in percent. The quality of this fit offers further evidence that propagating gravity waves are responsible for the density perturbations we observe.

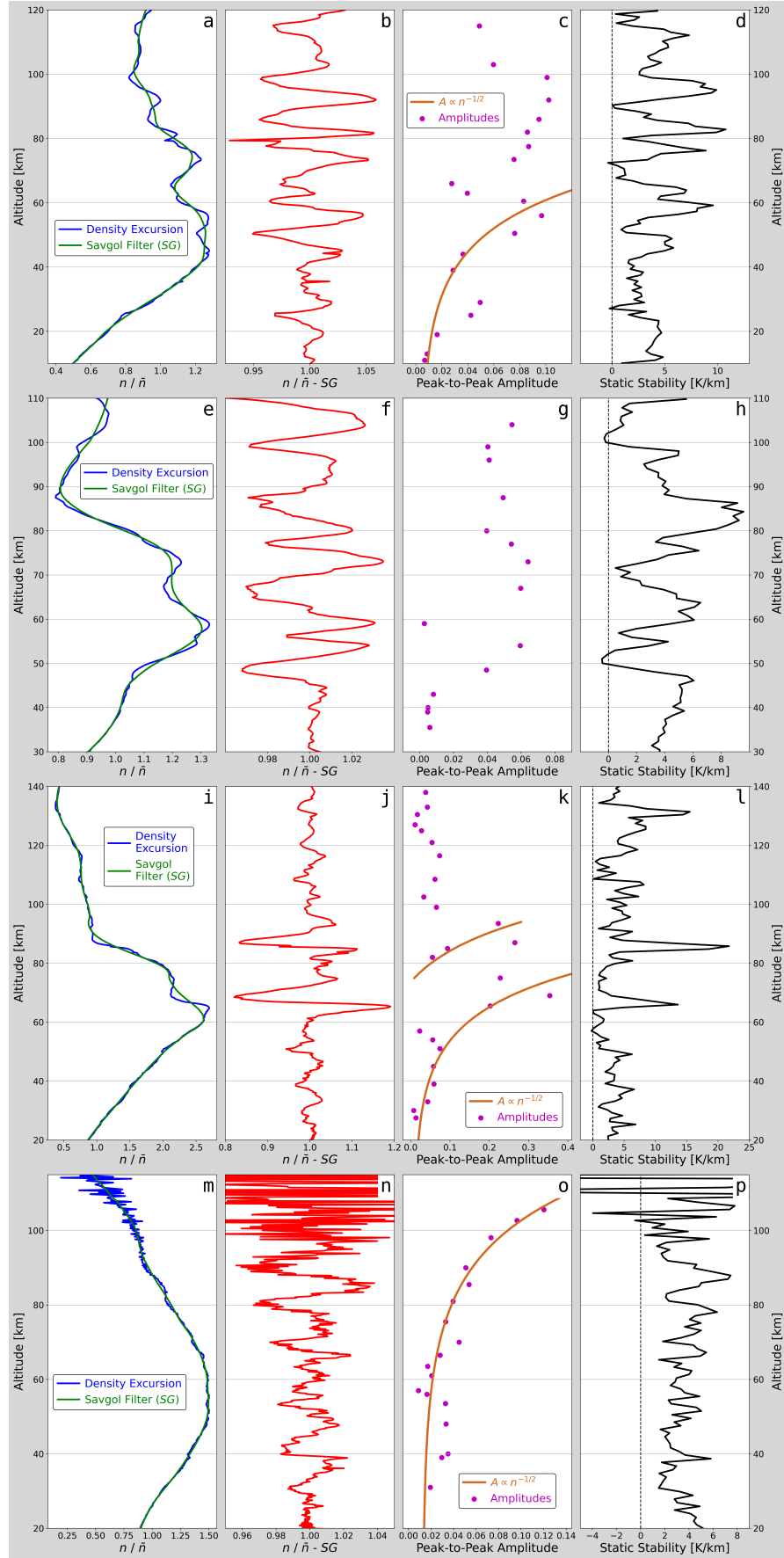


Figure 11. Entry profile wave results for Viking 1 (a–d), Viking 2 (e–h), Pathfinder (i–l), and Spirit (m–p). Columns are the same as in Figure 6 but with a 20 km savgol filter window.

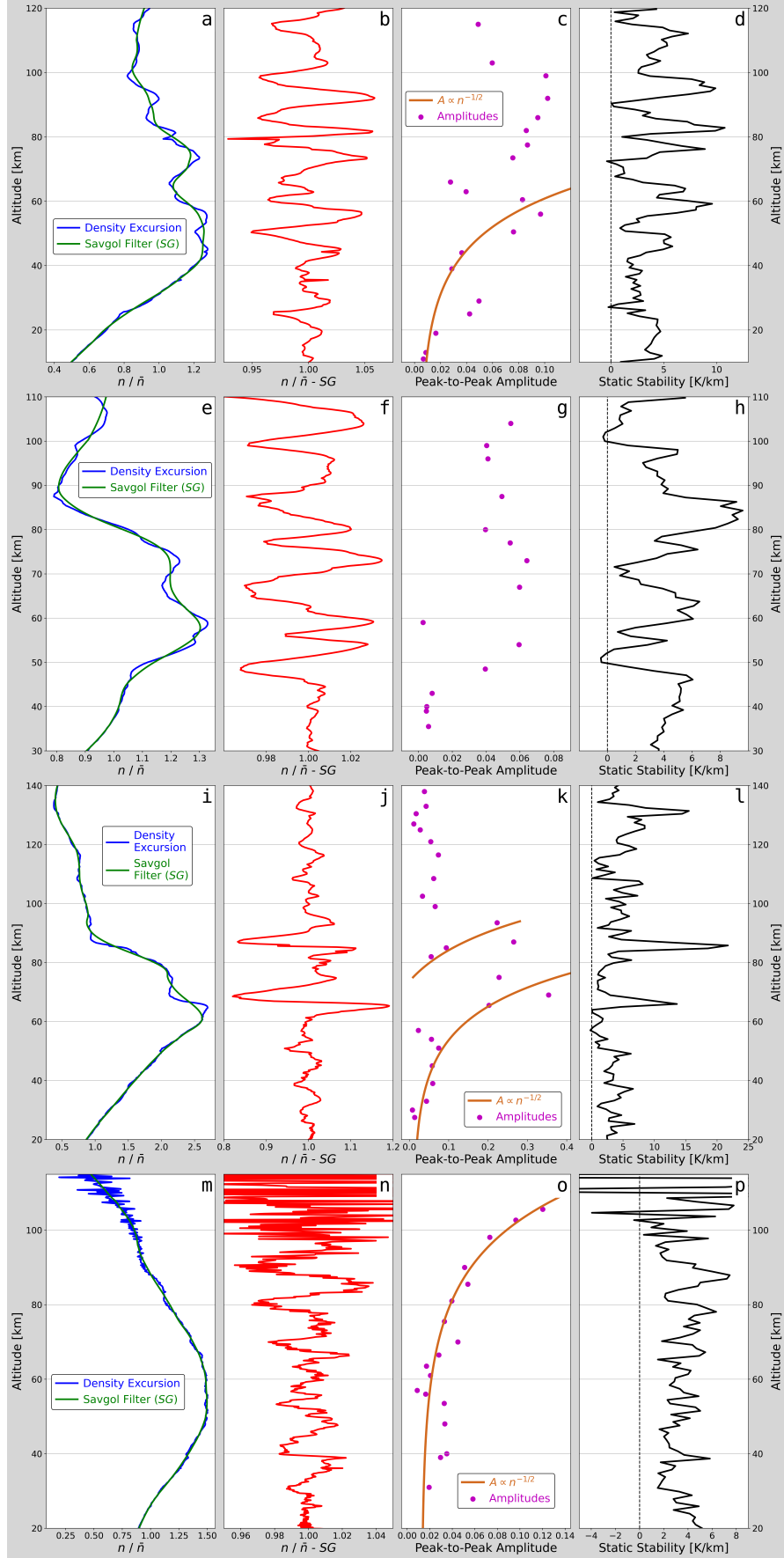


Figure 12. Entry profile wave results for Opportunity (a–d), Phoenix (e–h), Curiosity (i–l), and InSight (m–p). Columns are the same as in Figure 6 but with a 20 km savgol filter window.

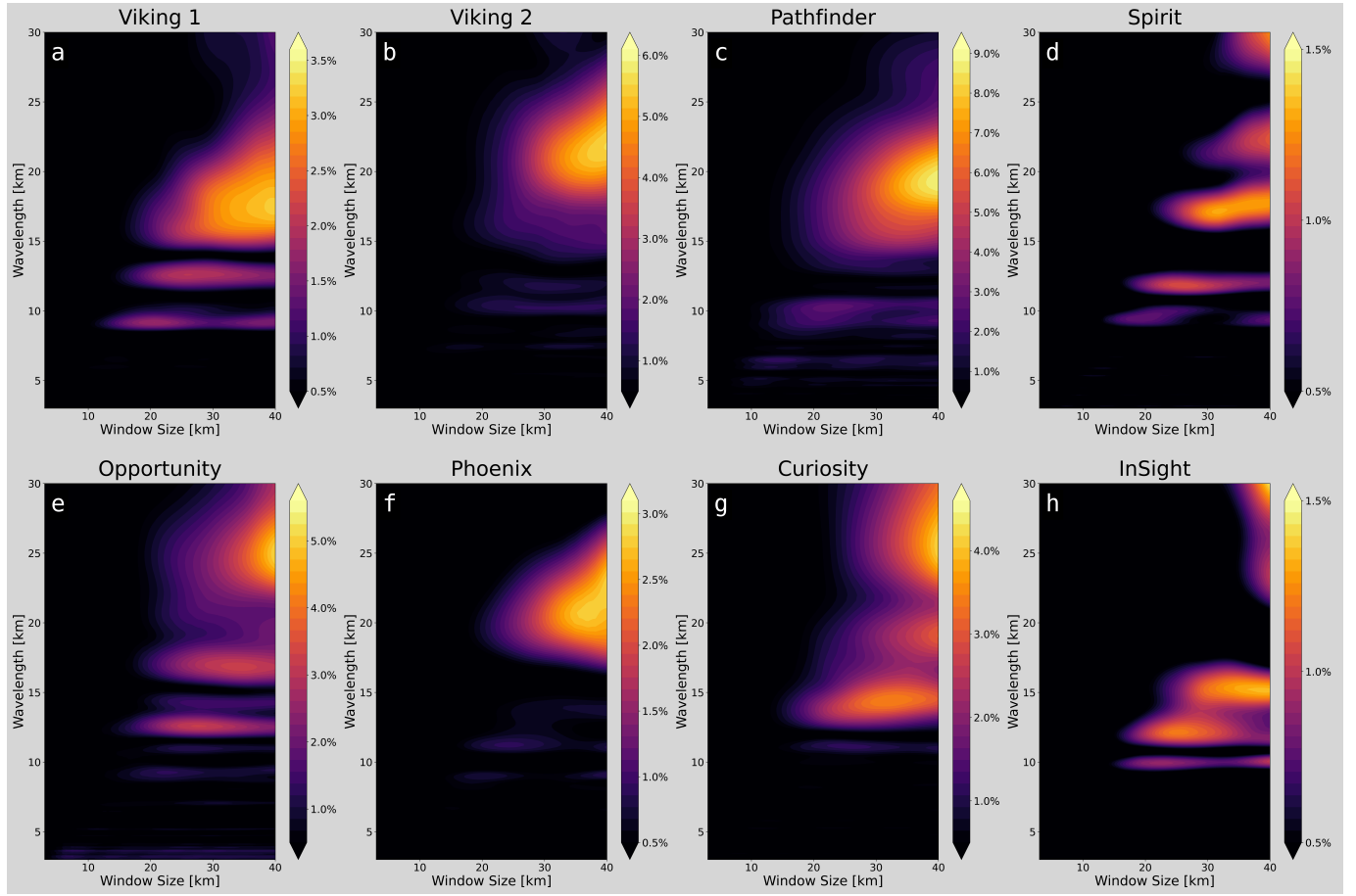


Figure 13. Amplitude spectra of all eight entry profiles represented as a contour plot, as in Figure 8. The features of wavelength greater than 15 km are likely thermal tides. The features of greatest interest are resolved best with a window size of 20 km.

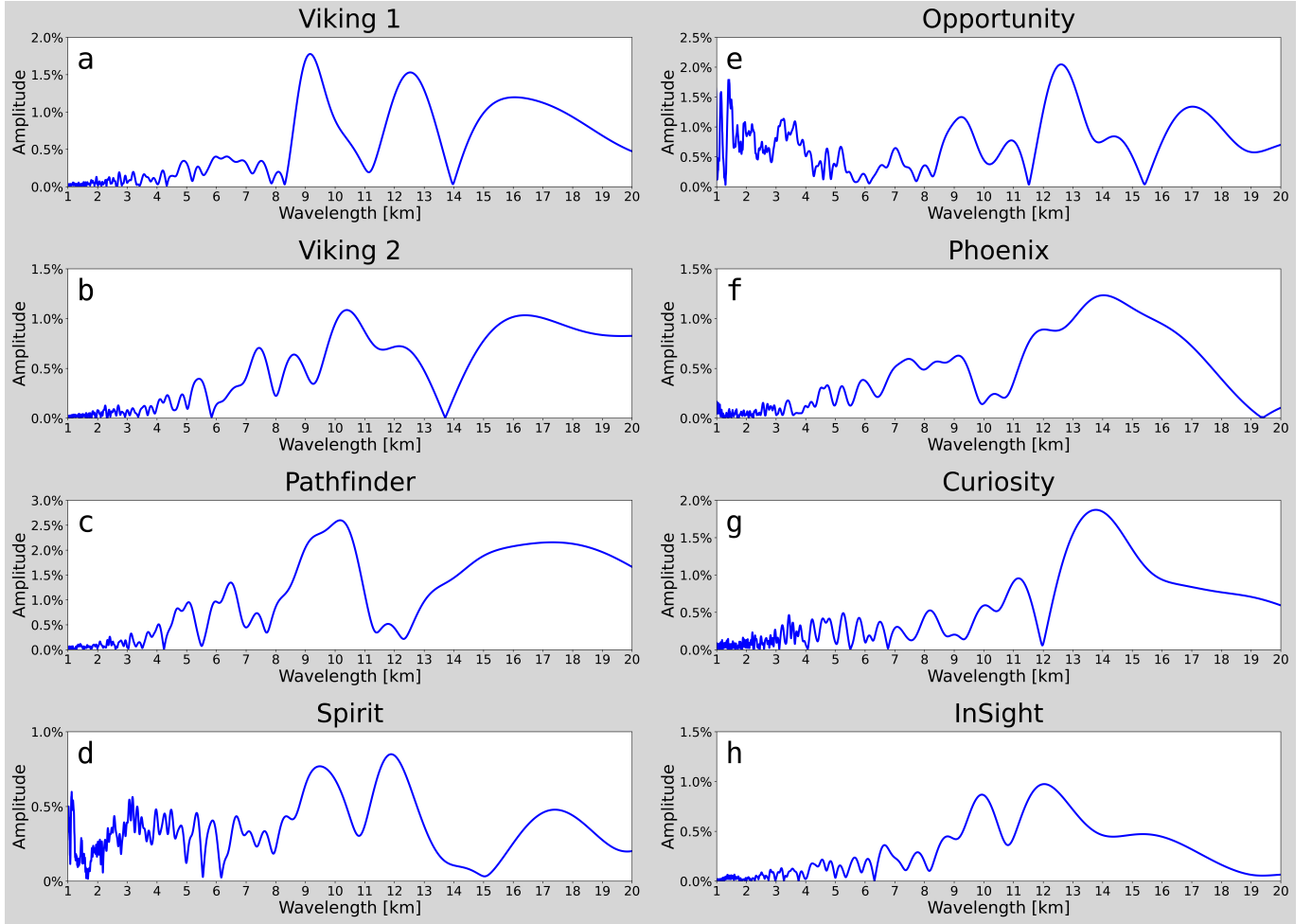


Figure 14. Amplitude spectra for all entry profiles with a savgol filter window of 20 km. The 20 km window highlights features representative of small-scale atmospheric waves. Dominant patterns in the amplitude spectra include peak wavelengths in the range 9–14 km, single- and double-peaked features, and peak amplitudes in the range 1–3%.

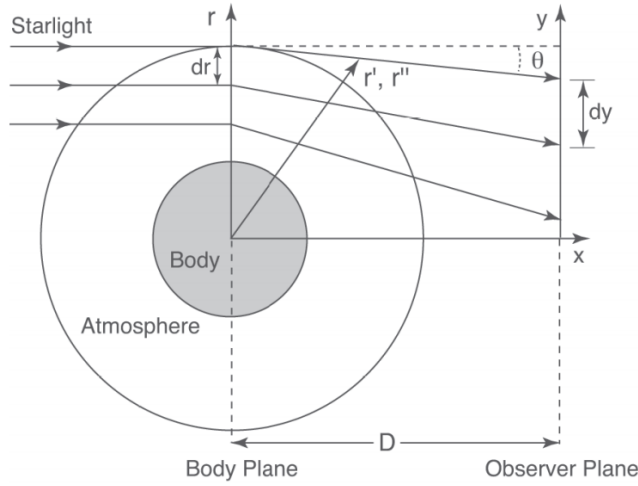


Figure 15. Refraction of starlight through a small body atmosphere. In this frame of reference, the target body is stationary and the star and observer move. The rays of starlight passing through spherical shells of the occulting body's atmosphere at radius r bend by angle θ before being observed on the right side of the diagram at relative observer distance y . The observer-body separation is given by D . r' and r'' serve as variables of integration. From [Elliot, Person, & Qu \(2003\)](#).

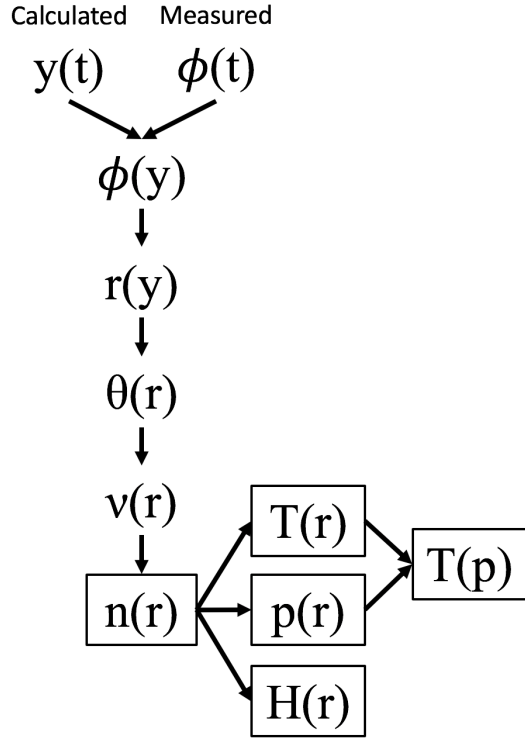


Figure 16. Flowchart showing the steps of inversion. Observer position $y(t)$ is determined as a function of time from the occultation geometry and flux $\phi(t)$ is measured as a time series. The important atmospheric properties are boxed: number density $n(r)$, temperature $T(r)$, pressure $p(r)$ and scale height $H(r)$ as a function of radius, and temperature as a function of pressure $T(p)$. After [Elliot, Person, & Qu \(2003\)](#).

Table 1. Model Fitting Parameter Results

Curve	Scale Height km	Temperature K	Ellipticity	Impact Parameter km	Reduced χ^2
Immersion	8.29 ± 0.29	154.8 ± 5.41	-	-	0.962
Emersion	6.55 ± 0.26	122.3 ± 4.86	-	-	1.034
Central flash	-	-	$2.53 \times 10^{-3} \pm 6.8 \times 10^{-5}$	22.1 ± 0.23	1.271

Table 2. Conditions During Obtained Data Acquisition

Data Source	Date and Time	Latitude ^a	Longitude ^b	L _s ^c	Local Time
		degrees	degrees	degrees	
Viking 1 ^d	1976-07-20 11:53:06	22.70	-48.22	97.2	14:25:46
Viking 2 ^d	1976-09-03 22:37:50	48.27	-225.99	117.9	13:03:54
Pathfinder ^e	1997-07-04 16:36:50.172	19.33	-33.55	143.0	08:22:56
Spirit ^f	2004-01-04 04:19:53.974	-14.57	175.48	327.9	12:25:12
Opportunity ^f	2004-01-25 04:48:43.605	-1.95	354.47	339.4	11:07:55
Phoenix ^g	2008-05-25 23:30:47.918	68.15	-125.90	76.9	11:34:50
Curiosity ^h	2012-08-06 05:10:42.924	-4.59	137.44	151.0	14:03:07
InSight ⁱ	2018-11-26 19:39:03.3441	4.50	135.62	296.0	03:42:26
Occultation Immersion ^j	1977-04-08 00:57:19.68	-27	-331	51.6	03:30
Occultation Emersion ^j	1977-04-08 01:02:34.01	28	-152	51.6	15:30

^a Positive is East.

^b Positive is North.

^c Planetocentric Longitude of the Sun.

^d Seiff & Kirk (1976)

^e Magalhães et al. (1999)

^f Withers & Smith (2006)

^g Withers & Catling (2010)

^h Holstein-Rathlou et al. (2016)

ⁱ Banfield et al. (2020)

^j Elliot et al. (1977b)

Table 3. Detected Wave Peaks

Profile	Wavelength	Peak Amplitude
km		
Immersion Ch. 2	3.4 ^a	0.93%
	4.1 ^a	0.70%
	5.7 ^a	1.1%
	9.4 ^a	2.7%
	12.5 ^b	2.2%
Immersion Ch. 3	3.4 ^a	0.61%
	4.1 ^a	0.94%
	6.1 ^b	0.82%
	10.0 ^a	3.4%
Emersion Ch. 2	5.4 ^a	0.93%
	10.3 ^b	1.4%
Emersion Ch. 3	5.6 ^b	0.50%
	8.9 ^a	1.6%
	13.7 ^a	2.4%
Viking 1	9.2	1.8%
	12.5	1.5%
	16.0	1.2%
Viking 2	10.4	1.1%
	16.4	1.0%
Pathfinder	10.2	2.6%
	17.3	2.2%
Spirit	9.5	0.77%
	11.9	0.85%
Opportunity	9.2	1.2%
	12.6	2.0%
	17.0	1.3%
Phoenix	9.0	0.75%
	11.2	0.79%
	19.6	0.72%
Curiosity	11.2	0.96%
	13.8	1.9%
InSight	9.9	0.87%
	12.0	0.98%

^a Confidence of $\geq 95\%$.^b Confidence of $\geq 99.99\%$.